Heliyon 11 (2025) e42603

Contents lists available at ScienceDirect

Heliyon

journal homepage: www.cell.com/heliyon

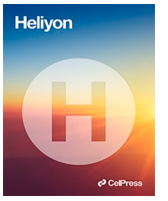

Research article

Dynamic tuning of optoelectronic and mechanical properties in $TlMCl_3$ (M = Ge, Sn) under pressure-induced phase transition

M.H. Mia [a,c,*], Mst.A. Khatun [b]

[a] Department of Textile Engineering, Northern University Bangladesh, Uttara, Dhaka, 1230, Bangladesh
[b] Department of Physics, Hajee Mohammad Danesh Science and Technology University, Dinajpur, 5200, Bangladesh
[c] Department of Computer and Communication Engineering, International Islamic University Chittagong Kumira, Chattogram, 4318, Bangladesh

ARTICLE INFO

Keywords:
DFT simulations
Electronic structure
Optical and dielectric properties
Mechanical characteristics

ABSTRACT

Recent advances in lead-free halide perovskites have expanded their potential use in solar panels and optoelectronic applications. Motivated by their excellent properties, we investigate the physical characteristics of two lead-free halide perovskites, $TlMCl_3$ (M = Ge, Sn), under hydrostatic pressure. This paper explores the pressure-induced semiconductor-to-metal phase transition in halide perovskites $TlMCl_3$ (M = Ge, Sn), focusing on their optoelectronic and mechanical properties. Using density functional theory (DFT), the study investigates structural, electronic, optical, and mechanical changes under hydrostatic pressures up to 6.5 GPa. Both $TlGeCl_3$ and $TlSnCl_3$ maintain a cubic perovskite structure, but exhibit decreasing lattice parameters and unit cell volumes with increased pressure. Electronic analyses reveal a transition from semiconducting to metallic states for both materials under pressure: $TlGeCl_3$'s band gap collapses to 0 eV at 6 GPa and $TlSnCl_3$ at 6.5 GPa according to TB-mbj, with GGA-PBE predicting transitions at 5 GPa for $TlGeCl_3$ and 3 GPa for $TlSnCl_3$. This transition is confirmed through partial density of states (PDOS) and band structure calculations. The SOC effect reduces the bandgap in $TlMCl_3$ (M = Ge, Sn), boosting their optoelectronic application potential. Enhanced dielectric constants and refractive indices under pressure improve their efficiency in solar cells and LEDs by reducing carrier recombination and strengthening photon-electron interactions. Their high transparency, UV reflectivity, and increased absorption and conductivity under pressure make them suitable for UV coatings, optical filters, and advanced optoelectronic devices. Mechanical analyses show improved stiffness and ductility, with $TlSnCl_3$ demonstrating excellent machinability. The pressure-enhanced ductility of $TlMCl_3$ (M = Ge, Sn) makes it suitable for flexible electronics, wearable devices, and robust solar cells. Furthermore, their outstanding photovoltaic potential is driven by large optical absorption and high charge carrier mobility, aided by their small effective masses.

1. Introduction

The interest in perovskite-type compounds stems from their versatility, making them valuable in industries ranging from semiconductors and superconductors to solar energy systems, optoelectronics, and LEDs[1–3]. The combination of excellent optoelectronic characteristics, economic viability, and environmental friendliness makes them essential for advancing efficient and sustainable

* Corresponding author. Department of Textile Engineering, Northern University Bangladesh, Uttara, Dhaka, 1230, Bangladesh
E-mail address: mdhasan111.ru@gmail.com (M.H. Mia).

https://doi.org/10.1016/j.heliyon.2025.e42603
Received 30 August 2024; Received in revised form 21 January 2025; Accepted 10 February 2025
Available online 10 February 2025

technologies. Advancing technological applications relies on a thorough understanding of materials' physical properties, encompassing structural, electronic, optical, mechanical, and thermal aspects. First-principles calculations provide insights into the physical properties of various materials, with their results being corroborated by experimental data[4–6]. Halide perovskites are commonly expressed with the formula ABX_3 for simplicity, where "A" and "B" are metal cations, and "X" is a halogen anion [7]. Perovskite solar cells (PSCs) now exhibit a power conversion efficiency (PCE) of 22.1 %, reflecting substantial progress in their evolution [8]. Although lead-based perovskite solar cells currently boast the highest power conversion efficiency (PCE) of 25.2 %, they suffer from durability issues due to their susceptibility to UV radiation, moisture, temperature fluctuations, and humidity. The efficiency of lead is notable, but its toxic nature makes it a less desirable choice for practical use. Therefore, finding an effective substitute for lead is essential. To resolve these issues, scientists are exploring potential substitutes for lead among elements from group 14 of the periodic table, including silicon (Si), tin (Sn), and germanium (Ge) [9,10]. Perovskite solar cells (PSCs) incorporating lead (Pb), like $CH_3NH_3PbI_3$ ($MAPbX_3$), were among the first to be developed and exhibited considerable promise[11–13]. Despite their potential, early Pb^{2+} -based organic PSCs were hindered by toxicity problems due to the hazardous nature of lead, presenting substantial disadvantages. Lead-free alternatives, like Sn halide perovskites with ethyl ammonium iodide, have achieved a power conversion efficiency (PCE) [14] of 13 %. Even with these developments, early PSCs containing organic MA^+ cations presented substantial ecological concerns, making the production process hazardous. Therefore, scientists have been focusing more on replacing Pb^{2+} with non-toxic cations like Ge^{2+} and Sn^{2+}, and on substituting organic A^+ cations with inorganic ones. The difficulty in producing lead-free halide-based perovskites is still a major hindrance to the extensive commercial deployment of perovskite-based solar cells.

Reducing the band gap in perovskite materials opens the door to enhanced light absorption, making it a key factor in boosting solar cell efficiency. This tuning can be achieved through various methods, such as temperature-induced phase transitions [15], chemical modifications [16,17], metal doping, and notably, hydrostatic pressure. Among these, hydrostatic pressure emerges as a particularly green, straightforward, and powerful tool for precisely altering the band gap of perovskites. Unlike ambient conditions, applying pressure can fundamentally transform these materials, fine-tuning the band gap, enhancing light absorption, minimizing charge carrier recombination, and optimizing charge separation. For example, when subjected to pressures of 0–8 GPa, the band gap of $KMCl_3$ (M = Ge, Sn) significantly decreases, enhancing conductivity and shifting the material from semiconductor to metallic states [18]. This change highlights the potential of these perovskites for optoelectronic devices in the visible and ultraviolet ranges. Similarly, applying hydrostatic pressure to $GaGeX_3$ (X = Cl, Br, I) allows for tunable band gap properties, resulting in improved absorption coefficients and exceptional optical conductivity across both visible and UV regions [19]. This pressure-driven modification not only enhances their optical properties but also significantly improves their performance in optoelectronic devices. Moreover, DFT calculations for lead-free halide perovskites like $AGeF_3$ (A = K, Rb) show that increasing pressure tightens the band gap, further amplifying their optical characteristics and making them ideal candidates for advanced solar cell applications [20]. In addition to reducing the band gap, hydrostatic pressure can also convert an indirect band gap into a direct one, which has been observed in several cubic perovskites [21–24]. This transformation significantly enhances their efficiency in absorbing light and converting it into electricity. For example, applying pressure to $CsBX_3$ (B = Sn, Ge; X = Cl, Br) reduces the band gap to zero, causing a transition from semiconductor to metal [25–29]. This switching from semiconductor to metal enhances the optical and mechanical properties of perovskite materials[25–29], making them highly suitable for advanced optoelectronic applications. In a related study, M. Miri et al. explored the effects of pressure (0–20 GPa) on $XZnF_3$ (X = Na, K, Rb) halide perovskites using DFT with GGA in Wien2k. Their findings reveal that pressure not only enhances material stability by increasing indirect band gaps and threshold energies but also reduces optical absorption intensity, highlighting a trade-off between stability and optical performance [30].

In this study, we focus on the potential of $TlMCl_3$ (M = Ge, Sn) halide perovskite compounds as promising candidates for advanced technological applications. The synthesis of $TlSnX_3$ (X = Cl, Br, I) by W. Kim et al. [31] has opened new avenues for exploring its diverse properties, while theoretical investigations on $TlGeCl_3$ have also gained traction. Rony et al. [32] have provided a comprehensive theoretical analysis of the structural, electronic, optical, elastic, mechanical, and anisotropic features of $TlBX_3$ (B = Ge, Sn; X = Cl, Br, I) at ambient pressure. Their findings highlight the excellent optical properties of these compounds, making them ideal for applications in solar cells, light-emitting diodes (LEDs), and photodetectors. Further contributions from Pooja et al. [33] have calculated the structural, electronic, optical, and thermal properties of $TlZX_3$ (Z = Ge, Sn, Be, Sr; X = Cl, Br, I) using DFT and TD-DFT approaches. Their results indicate that the computed energy gap and refractive index suggest potential applications in scintillators and solar cells. Marjaou et al. [34] expanded on this work by investigating the mechanical and optical properties of $TlGeX_3$ (X = F, Cl) under hydrostatic pressures up to 25 GPa. They found that these perovskites exhibit significant absorption properties and a transition from semiconductor to metallic states, positioning them as promising candidates for solar cells and ultraviolet absorbers. In addition, Bouhmaidi et al. [35] examined the structural, electronic, elastic, optical, and thermoelectric properties of $TlGeX_3$ (X = Cl, Br, I) to evaluate their potential applications in optoelectronic and thermoelectric devices at ambient pressure. Pingak et al. [36] also contributed by investigating the structural parameters and electronic properties of $TlGeCl_xBr_{3-x}$ (x = 0, 1, 2, 3) to assess their viability as absorbers in perovskite solar cells using Density Functional Theory (DFT) within the Quantum Espresso framework. The results demonstrated the promising nature of these compounds as lead-free alternatives for perovskite solar cells.

Despite these advancements, research on the pressure dependence of physical properties in $TlMCl_3$ (M = Ge, Sn) remains limited. Hydrostatic pressure is a well-established method for thoroughly investigating the physical properties of perovskites. Thus, this study aims to clarify these aspects and serve as a guide for future research. Our primary goal is to determine the critical pressure at which $TlMCl_3$ (M = Ge, Sn) transitions from a semiconductor to a metallic state and to explore how other key properties evolve under varying pressures. Notably, we observe that the band gap decreases with increasing hydrostatic pressure, and this application significantly enhances optical properties, which are vital for optoelectronic applications. Our findings reveal that the semiconductor-to-metal phase transition occurs at 6 GPa for $TlGeCl_3$ and at 6.5 GPa for $TlSnCl_3$, according to the TB-mbj approach. Hence, we focus on a specific

hydrostatic pressure range of 0–6.5 GPa to comprehensively study these transitions. By investigating a pressure range of 0–6.5 GPa, we focus on how the electronic, optical, and mechanical properties evolve under applied pressure. The switching from semiconductor to metal not only enhances optical characteristics but also improves mechanical properties, making these perovskites more suitable for advanced optoelectronic applications. Our research underscores the significance of hydrostatic pressure in tuning the properties of $TlMCl_3$ (M = Ge, Sn). The unique attributes of these compounds, such as low effective masses, high conductivity, and strong absorption, position them as excellent candidates for photovoltaic applications. Moreover, pressure-enhanced ductility suggests potential uses in flexible electronics and wearable devices. The ongoing exploration of $TlMCl_3$ (M = Ge, Sn) under pressure promises to reveal valuable insights into its suitability for next-generation solar cells and other cutting-edge optoelectronic devices. We eagerly anticipate experimental validations of our findings in the near future.

2. Computational methodology

In this study, we employ a combination of advanced computational methods to estimate the structural, electronic, optical, and mechanical properties of $TlMCl_3$ (M = Ge, Sn). The primary tool for these simulations is the Cambridge Serial Total Energy Package (CASTEP) [37], which operates within the framework of density functional theory (DFT) [38]. Specifically, we use the generalized gradient approximation (GGA) with the Perdew-Burke-Ernzerhof (PBE) functional to approximate the exchange-correlation energy of electrons, a crucial aspect for accurate simulations [39]. For the plane-wave basis set, we define a cut-off energy of 550 eV. The convergence tolerances are set as follows: 5×10^{-6} eV/atom for total energy, 5×10^{-4} Å for maximum displacement, 0.01 eV/Å for maximum force, and 0.02 GPa for maximum stress. Integration over the Brillouin zone is performed using a $12 \times 12 \times 12$ *k*-point grid following the Monkhorst-Pack scheme [40] to ensure accurate sampling of the reciprocal space. To model the electron-ion interactions, Vanderbilt-type ultrasoft pseudopotentials are utilized [41]. We employ the Broyden-Fletcher-Goldfarb-Shanno (BFGS) [42] method to optimize the crystal structure, relaxing both lattice parameters and atomic positions to find the lowest energy configuration. Hydrostatic pressures ranging from 0 to 6.5 GPa are applied to optimize the crystal structure and evaluate various physical properties under different pressure conditions. The optimized crystal structures are visualized using the VESTA software [43]. CASTEP is also used to calculate elastic constants and moduli using the 'stress-strain' method. For electronic properties, the WIEN2k code [44] is employed with the Tran-Blaha modified Becke-Johnson (TB-mBJ) [45] potential. This hybrid potential is chosen for its enhanced accuracy in predicting band gaps, particularly in systems with *d* or *f* orbital electrons. Charge and energy convergence are ensured by using a plane-wave expansion parameter $R_{MT} \times K_{max} = 7$, and a Fourier series expansion up to $G_{max} = 12$ a.u^{-1} in the interstitial region. For detailed electronic and optical property calculations, a dense$17 \times 17 \times 17$ *k*-point mesh is used for Brillouin zone integrations.

3. Results and discussion

3.1. Structural properties

The halide perovskites $TlMCl_3$ (M = Ge, Sn) are conventional ABX_3 perovskites with a cubic crystallographic structure classified under the space group *Pm*-3*m* (#221). In this structure, the Tl, Ge/Sn, and Cl atoms occupy the corner, body center, and face center positions of the unit cell, respectively. Specifically, the Wyckoff positions for Tl, Ge/Sn, and Cl are 1a (0, 0, 0), 1b (0.5, 0.5, 0.5), and 3c (0, 0.5, 0.5), respectively. Fig. 1 illustrates the optimized crystal structure with these crystallographic sites. After structural optimization, the calculated lattice parameters for $TlGeCl_3$ and $TlSnCl_3$ are provided in Table 3. These values closely match previous reports at ambient pressure [32]. Notably, the optimized lattice constant for $TlSnCl_3$ (5.558 Å) is larger than that for $TlGeCl_3$ (5.231 Å) at ambient pressure, which can be attributed to the larger atomic radius of Sn compared to Ge. The compounds were subjected to hydrostatic pressure ranging from 0 to 6.5 GPa. Fig. 3(a and b) show that both the lattice parameter and unit cell volume decrease smoothly with increasing applied hydrostatic pressure. This trend suggests a reduction in the bond length between atoms in both compounds (see Fig. 4(a and b)), leading to a stronger repulsive force between atoms. This, in turn, enhances the crystal hardness under elevated pressure. In halide perovskites, with the general formula ABX_3, the A-X and B-X bonds play distinct roles in determining the material's properties. The A-site cation stabilizes the perovskite structure, residing at the top corner of the cubic unit cell.

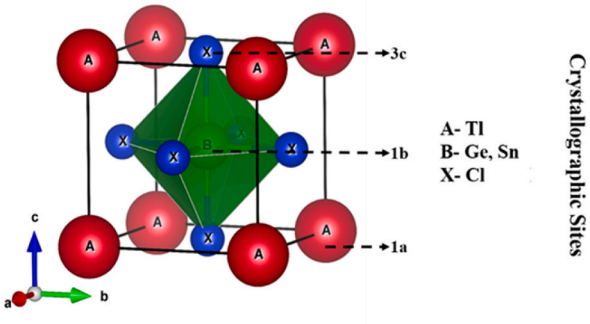

Fig. 1. Visualization of the cubic perovskite structure of $TlMCl_3$ (M = Ge, Sn) with annotated crystallographic sites.

Therefore, understanding the nature of A-X (Tl-Cl) and B-X (Ge-Cl, Sn-Cl) bonds is crucial for analyzing the material's solid-state properties. The B-X bond is particularly important, as it governs the photovoltaic properties of these halide perovskites [46]. We calculated the Tl-Cl, Ge-Cl, and Sn-Cl bond lengths under increasing pressure, as shown in Table 1, providing critical insights into how these bonds evolve and influence the material's optoelectronic performance. Similar behavior has been observed in other cubic halide perovskites, such as $RbSnX_3$ (X = Cl, Br) [47], $RbGeX_3$ (X = Cl, Br) [48], $KCaCl_3$ [49], and $CsCaBr_3$ [50].

To harness the advanced capabilities of the WIEN2k code, we conducted an optimization of the structural parameters for the cubic perovskites $TlGeCl_3$ and $TlSnCl_3$ in their non-magnetic (NM) and ferromagnetic (FM) phases. The optimization process relied on Energy vs. Volume calculations, which revealed critical insights into the compounds' structural stability. The energetically stable configuration was determined using the Birch-Murnaghan equation [51,52].

$$E(V) = E_0 + \frac{B}{B'(B'-1)}\left[V\left(\frac{V_0}{V}\right)^{B'} - V_0\right] + \frac{B}{B'}(V - V_0) \tag{1}$$

Here, E is the total energy per unit cell, E_0 is the ground-state energy, V_0 is the equilibrium unit cell volume (defined by $a = b = c$), B is the bulk modulus, and B' is the pressure derivative of the bulk modulus.

The state with the lowest energy in the Energy vs. Volume curve represents the most stable configuration. Our analysis (Fig. 2(a and b)) clearly shows that $TlGeCl_3$ and $TlSnCl_3$ are more stable in their NM phase than in the FM phase, as the NM phase exhibits lower energy ($E_{NM} < E_{FM}$). This NM stability aligns well with prior Density Functional Theory (DFT) studies, affirming the compounds' non-magnetic nature [53,54].

To further validate the stability of $TlMCl_3$ (M = Ge, Sn) under pressure, we evaluated their formation energy and cohesive energy, key indicators of thermodynamic stability. These calculations provide a deeper understanding of the materials' structural robustness and suitability for practical applications. The formation energy (ΔE_f) of $TlMCl_3$ (M = Ge, Sn) was calculated using the following equation [52]:

$$\Delta E_f(TlMCl_3) = \frac{[E_{tot.}(TlMCl_3) - E_s(Tl) - E_s(M) - 3E_s(Cl)]}{N} \tag{1}$$

Additionally, the cohesive energy (E_{coh}) was calculated by using the following expression [55]:

$$E_{coh} = -\frac{E_{tot} - [n_{Tl}E(Tl) + n_M E(M) + n_{Cl}E(Cl)]}{n_{Tl} + n_M + n_{Cl}} \tag{2}$$

In this equation, E_s(Tl), E_s(M), and E_s(Cl) represent the energy values of Tl atoms, M (Ge, Sn) atoms, and Cl atoms, respectively. $\boldsymbol{E_{tot.}}(\mathbf{TlMCl_3})$ denotes the total energy of the unit cell of $TlMCl_3$ (M = Ge, Sn), and N is the total number of atoms in the unit cell. The terms $\boldsymbol{n_{Tl}}$, $\boldsymbol{n_M}$, and $\boldsymbol{n_{Cl}}$ denote the number of Tl, M (Ge, Sn), and Cl atoms within the unit cell.

The calculated formation energy, cohesive energy, and total ground-state energies under pressure, as summarized in Table 2. The negative values of formation enthalpy observed for both compounds strongly affirm their stability under the investigated pressure conditions. These results are consistent with cohesive energy and ground-state energy calculations, which further reinforce the conclusion that $TlMCl_3$ (M = Ge, Sn) perovskites exhibit excellent thermodynamic stability under pressure. Thermodynamic stability in perovskites is highly desirable for several reasons: a stable compound is generally easier to synthesize, exhibits greater resistance to damage from factors such as radiation or heat, and can serve as a stabilizer in solid solutions of mixed perovskites [56].

In the study by Batool et al. [24], the Goldschmidt tolerance factor (t) is used to assess the stability of the cubic structure of $TlMCl_3$ (M = Ge, Sn) under varying pressures. The tolerance factor is calculated using the equation:

$$\boldsymbol{t} = \frac{\mathbf{0.707}\left(\boldsymbol{d^{Tl-Cl}}\right)}{\boldsymbol{d^{M-Cl}}} \tag{3}$$

According to Batool et al. [24], for a structure to be considered cubically stable, its tolerance factor should fall within the range of 0.93–1.02. The analysis of Table 1 indicates that the calculated tolerance factors for $TlGeCl_3$ and $TlSnCl_3$ fall within the ideal range of

Table 1
Hydrostatic pressure effects on bond lengths (d) and Goldschmidt tolerance factors (t) in $TlMCl_3$ (M = Ge, and Sn).

Pressure (GPa)	Bond length (Å)				Tolerance factor (t)	
	$TlGeCl_3$		$TlSnCl_3$			
	d^{Tl-Cl}	d^{Ge-Cl}	d^{Tl-Cl}	d^{Sn-Cl}	$TlGeCl_3$	$TlSnCl_3$
0	3.69905	2.61563	3.93022	2.77908	0.999	0.999
1	3.65926	2.58749	3.88037	2.74384	0.999	0.999
2	3.62325	2.56202	3.83788	2.71379	0.999	0.999
3	3.59199	2.53992	3.79993	2.68696	0.999	0.999
4	3.56321	2.51957	3.76648	2.66331	0.999	0.999
5	3.53766	2.50150	3.73612	2.64184	0.999	0.999
6	3.51367	2.48454	3.70943	2.62296	0.999	0.999
6.5	3.50252	2.47666	3.69661	2.61390	0.999	0.999

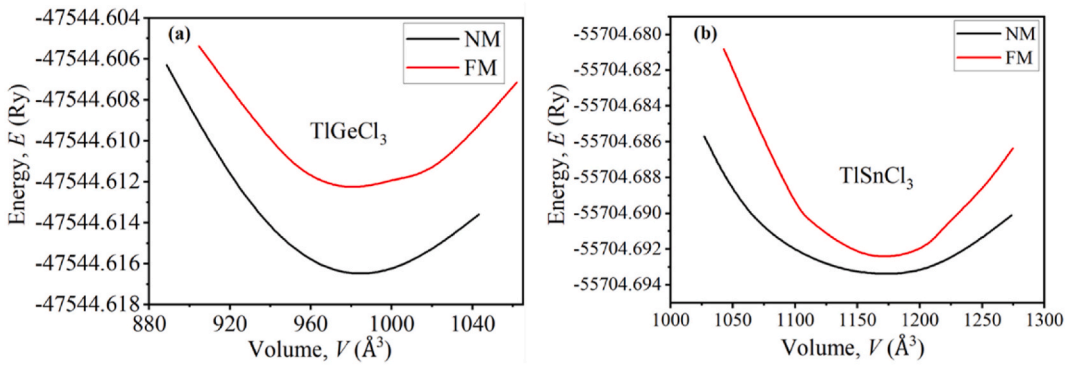

Fig. 2. The energy optimization as a function of unit cell volume for (a) $TlGeCl_3$, and (b) $TlSnCl_3$ halide perovskites in ferromagnetic and non-magnetic states.

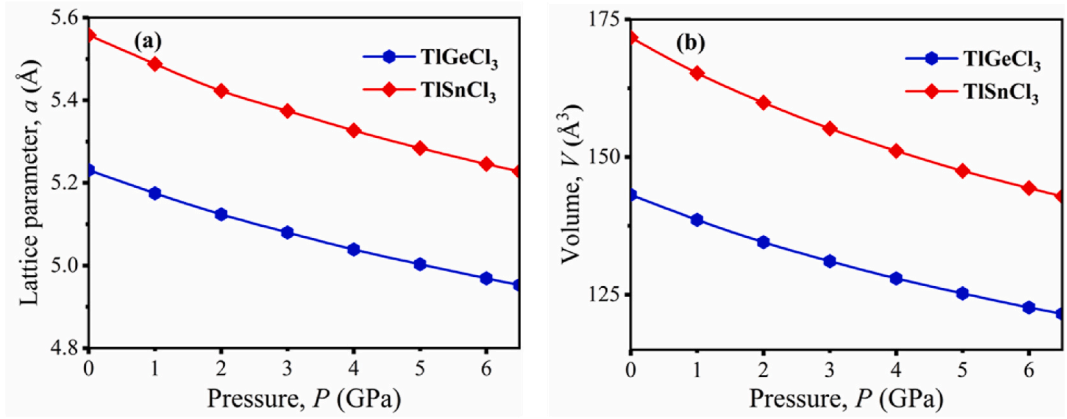

Fig. 3. Pressure-dependent variation of (a) lattice constant and (b) unit cell volume for $TlMCl_3$ (M = Ge, Sn).

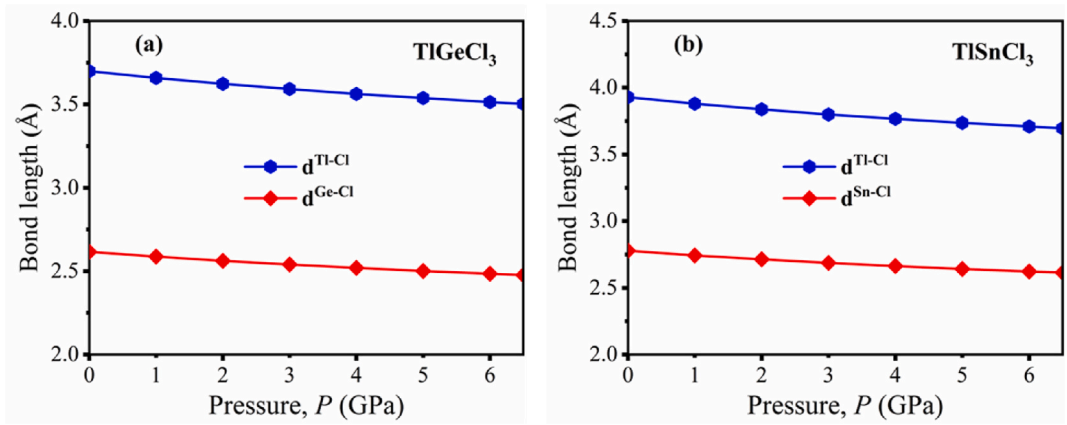

Fig. 4. Pressure-induced changes in bond lengths for (a) $TlGeCl_3$ and (b) $TlSnCl_3$.

0.93–1.02, thereby confirming that these compounds maintain cubic stability under the conditions studied.

3.2. Electronic properties

The features of the band structure play a key role in determining thermoelectric transport properties of a material. To explore how pressure influences the band structures, we analyzed $TlGeCl_3$ and $TlSnCl_3$ with and without pressure, plotting their band structures

Table 2
Thermodynamic stability parameters, including formation energy (ΔE_f), cohesive energy (E_{Coh}), and ground-state energy (E), for $TlGeCl_3$ and $TlSnCl_3$ perovskites under pressures ranging from 0 to 6.5 GPa.

Pressure (GPa)	Formation energy, ΔE_f (eV/atom)		Cohesive energy, E_{Coh} (eV/atom)		Ground state energy, E (eV)	
	$TlGeCl_3$	$TlSnCl_3$	$TlGeCl_3$	$TlSnCl_3$	$TlGeCl_3$	$TlSnCl_3$
0	−2.013	−2.104	−6.021	−6.321	−2713.2511	−2701.9126
1	−2.011	−2.100	−6.017	−6.316	−2713.2520	−2701.8931
2	−2.010	−2.094	−6.010	−6.309	−2713.2139	−2701.8429
3	−1.998	−2.084	−6.001	−6.301	−2713.1599	−2701.7709
4	−1.989	−2.072	−5.901	−6.290	−2713.0916	−2701.6822
5	−1.978	−2.058	−5.883	−6.280	−2713.0149	−2701.5804
6	−1.967	−2.044	−5.799	−6.265	−2712.9282	−2701.5804
6.5	−2.054	−2.130	−6.047	−6.345	−2713.9299	−2701.4199

Table 3
Comparison of calculated lattice constants (a), and unit cell volumes (V) for $TlMCl_3$ (M = Ge, Sn) at different hydrostatic pressures, incorporating available theoretical data.

Pressure (GPa)	a (Å)				V (Å^3)	
	$TlGeCl_3$		$TlSnCl_3$			
	This work	Previous work [32]	This work	Previous work [32]	$TlGeCl_3$	$TlSnCl_3$
0	5.231	5.262	5.558	5.573	143.158	171.710
1	5.175	–	5.488	–	138.588	165.259
2	5.124	–	5.423	–	134.536	159.890
3	5.080	–	5.374	–	131.084	155.194
4	5.039	–	5.327	–	127.957	151.131
5	5.003	–	5.284	–	125.226	147.505
6	4.969	–	5.246	–	122.696	144.367
6.5	4.953	–	5.228	–	121.531	142.875

along high symmetry points in the Brillouin zone. We first calculated the electronic band structures for $TlMCl_3$ (M = Ge, Sn) using the GGA-PBE functional. It is well established that standard DFT functionals often underestimate the band gaps of semiconductors. To overcome this limitation and achieve more accurate results, we employed the Tran-Blaha modified Becke-Johnson (TB-mBJ) potential in our calculations for $TlMCl_3$ (M = Ge, Sn). The TB-mBJ exchange potential [57] is known for effectively handling the exchange part of the exchange-correlation energy, enabling precise calculations of optoelectronic properties. This method has been widely recognized for delivering accurate bandgap estimations for semiconductors[57–60]. As a result, we have chosen to present only the graphs obtained using the TB-mBJ method to ensure the reliability and precision of our findings. The calculated band gap values are shown in Table 4 and the corresponding band structure visualizations in Fig. 5(a and b) and **6(a, b)** offer a comprehensive insight into the impact of hydrostatic pressure on the electronic properties of $TlGeCl_3$ and $TlSnCl_3$. The band gap values for $TlGeCl_3$ and $TlSnCl_3$ at ambient pressure align closely with previously reported results [32,34,61]. The computational results reveal that both the conduction band minimum (CBM) and the valence band maximum (VBM) are located at the R point in the Brillouin zone under applied pressure. This indicates that $TlMCl_3$ (M = Ge, Sn) possesses a direct band gap, a highly desirable feature for semiconductors. The direct alignment of the CBM and VBM enhances the efficiency of optical transitions, making these materials particularly promising for optoelectronic applications, including solar cells and light-emitting devices. At ambient pressure (0 GPa), the band gaps of $TlGeCl_3$ and $TlSnCl_3$ are found to be 0.840 eV and 0.792 eV, respectively, according to the GGA-PBE method. The TB-mBJ method, which is recognized for

Table 4
Variation of the electronic band gap (E_g) in $TlMCl_3$ (M = Ge, Sn) as a function of applied hydrostatic pressure.

Pressure (GPa)	Band gap (eV)					
	$TlGeCl_3$			$TlSnCl_3$		
	GGA-PBE	TB-mBJ	Previous study	GGA-PBE	TB-mBJ	Previous study
0	0.840	1.281	1.36 (TB-mBJ) [32] 0.91 (GGA) [32] 0.81 (GGA) [34]	0.792	1.346	1.19 (TB-mBJ) [32] 0.88 (GGA) [32] 0.82 (GGA) [61]
1	0.623	0.896	–	0.551	1.205	–
2	0.446	0.687	–	0.208	0.861	–
3	0.282	0.494	–	0	0.665	–
4	0.121	0.306	–	0	0.466	–
5	0	0.133	0 (GGA) [34]	0	0.272	–
6	0	0	–	0	0.095	–
6.5	0	0	–	0	0	–

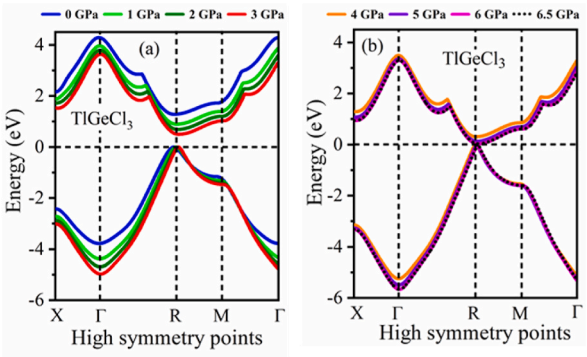

Fig. 5. Pressure-dependent electronic band structures of $TlGeCl_3$ for (a) 0 GPa, 1 GPa, 2 GPa, and 3 GPa, (b) 4 GPa, 5 GPa, 6 GPa, and 6.5 GPa.

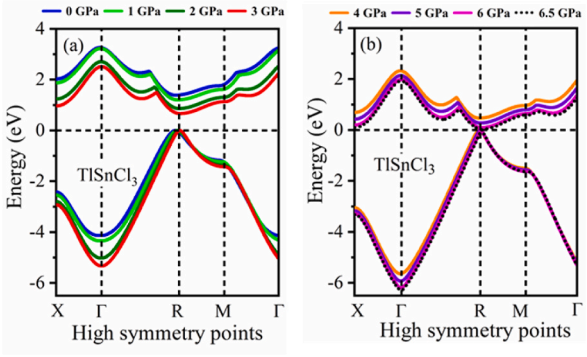

Fig. 6. Pressure-dependent electronic band structures of $TlSnCl_3$ for (a) 0 GPa, 1 GPa, 2 GPa, and 3 GPa, (b) 4 GPa, 5 GPa, 6 GPa, and 6.5 GPa.

providing more accurate band gap estimates, reports slightly higher values of 1.281 eV for $TlGeCl_3$ and 1.346 eV for $TlSnCl_3$, respectively. As hydrostatic pressure is incrementally applied, both materials exhibit a steady decrease in their band gaps. For $TlGeCl_3$, the band gap progressively narrows, ultimately reaching 0 eV at 5 GPa when using the GGA-PBE method, signaling a transition to a metallic state. A similar trend is observed with the TB-mBJ method, where the band gap closes completely at 6 GPa. On the other hand, $TlSnCl_3$ follows a comparable pattern, with its band gap reducing to 0 eV at 3 GPa using GGA-PBE and at 6.5 GPa using TB-mBJ. The data also reveal that the TB-mBJ method consistently predicts higher band gap values compared to GGA-PBE, highlighting its reliability and accuracy in electronic structure calculations. As pressure increases, the conduction band minimum (CBM) of both perovskites gradually shifts towards the Fermi level, while the valence band maximum (VBM) remains fixed at the R-point, causing a significant reduction in the band gap (E_g). This effect is further amplified by the increasing potential between electrons and ions, which compresses the lattice parameters due to the inverse relationship with the band gap [62] (see Fig. 6).

When pressure is applied to a crystalline material, it reduces the interatomic distances, causing atoms to shift positions without altering their relative arrangement. This brings the ions in the valence band (VB) and conduction band (CB) closer together. As a result, the band gap decreases, and in some cases, the two bands may even overlap. Our calculations reveal this effect in the electronic band

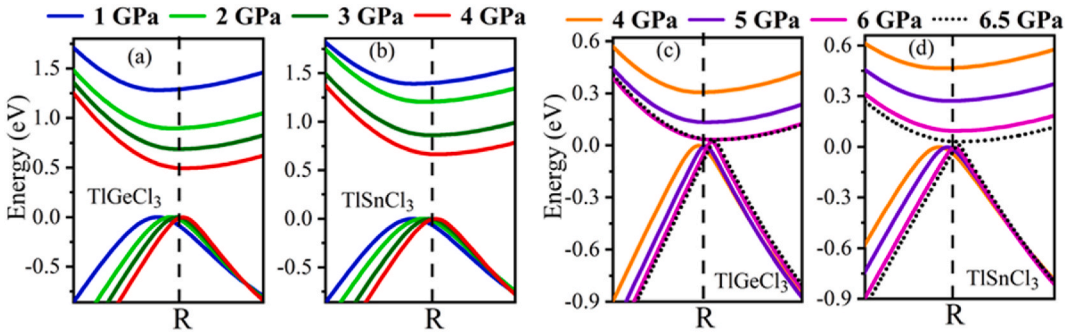

Fig. 7. (a–d). Pressure-dependent variation of the band gap at the R-point for $TlMCl_3$ (M = Ge, Sn), illustrating the impact of hydrostatic pressure on electronic properties.

structure diagram (Fig. 7(a-d)). The reduction in lattice parameters enhances the overlap of electronic orbitals, especially the *p* orbitals in the conduction band and *s* or *p* orbitals in the valence band, facilitating electron transport. Notably, similar transitions to metallic behavior under pressure have been observed in previous studies[25–29], confirming the validity of this analysis. Our study reveals that the band gap decreases gradually from 0 GPa to 6.5 GPa for both compounds. At higher pressures, the conduction and valence bands begin to overlap at the Fermi level (E_F), effectively closing the band gap. This transition implies a shift from semiconductor to metallic behavior, enhancing the material's conductivity. This pressure-induced transition leads to an increased absorption coefficient in the visible region, as shown in Fig. 12(b). The pressure-induced narrowing of the band gap facilitates electron transport, making $TlMCl_3$ (M = Ge, Sn) highly tunable under pressure and promising for advanced optoelectronic applications requiring efficient charge carrier mobility.

Pressure-induced metallization offers exciting potential for the development of innovative electronic devices, such as high-pressure switches or sensors. This phenomenon, observed in other materials, lends strong support to our findings. For example, X. Chen et al. demonstrated intrinsic capacitor-like faradaic charge storage in $FeS_{1-x}Se_x$ ($x \geq 0.5$) through a semiconductor-to-metal transition, even in bulk crystalline form [63]. Similarly, A. C. M. Esther et al. explored this transition in V_2O_5, revealing its promising applications in optoelectronics, plasmonics, and photonics [64]. In the case of $TlMCl_3$ (M = Ge, Sn), while the material exhibits a band-gap energy under ambient pressure, applying pressure could effectively tune this band gap, leading to metallization, as predicted by theoretical calculations. This opens the door for further systematic investigations into the electrical properties of $TlMCl_3$ (M = Ge, Sn) under high-pressure conditions to confirm whether the semiconductor-to-metal transition indeed occurs. We hope these findings inspire future experimental studies to verify and expand upon our predictions, advancing the field of pressure-induced metallization.

In optoelectronic device technology, understanding effective mass is essential. It represents the mass of an electron or hole in a semiconductor, influencing mobility and performance. Materials with low effective masses are ideal for optoelectronic applications, as they enhance charge carrier transport and boost device efficiency [35]. The effective mass reflects the curvature of the electronic bands near the conduction band minimum (CBM) and valence band maximum (VBM). These effective masses are derived from the curvature of the electronic band structure. A smaller curvature leads to larger effective masses, and vice versa. Fig. 7(a-d) offers an enlarged view of the band structure near the Fermi energy (E_F) at *R*-point for $TlMCl_3$ (M = Ge, Sn). The flat band structure in the conduction band of $TlGeCl_3$ and $TlSnCl_3$ perovskites is notable. Their valence bands show a parabolic nature (see Fig. 7(a-d)). This feature is common in thallium-based perovskites[65–67]. This flat band structure is linked to strong anharmonicity, which contributes to high thermoelectric performance [66]. Due to these properties, $TlMCl_3$ (M = Ge, Sn) shows significant potential for thermoelectric applications. As pressure increases from 0 to 6.5 GPa, the valence bands become more parabolic, indicating enhanced hole mobility. Meanwhile, the conduction bands show a slight steepening along the *R*-point, suggesting subtle changes in electron transport. The more parabolic valence band under pressure suggests better hole transport, which improves charge separation and reduces recombination losses. This results in more efficient charge extraction and higher open-circuit voltage, enhancing photovoltaic device performance [68]. Meanwhile, the slight steepening of the conduction band implies shifts in electron transport. Despite the heavier electrons, sufficient mobility is maintained, making these materials suitable for pressure-tunable optoelectronic devices.

Since $TlGeCl_3$ and $TlSnCl_3$ are direct bandgap semiconductors, we focus on the conduction band minimum (CBM) and valence band maximum (VBM) at the *R*-point. The effective masses m^* are computed as follows [69]:

$$m^* = \frac{\hbar^2}{\left(d^2E/dk^2\right)} \tag{4}$$

where *E* represents the band-edge energy and *k* is the reciprocal lattice vector. By fitting *E-k* states at the VBM and CBM for $TlMCl_3$ (M = Ge, Sn), we calculated the electron and hole effective masses.

The relationship between carrier mobility (μ) and effective mass (m^*) is important in understanding transport behavior of semiconductor materials. Since carrier mobility is inversely proportional to effective mass ($\mu \propto \frac{1}{m^*}$), an increase in effective mass directly lowers mobility and reduces electrical conductivity [70]. The Drude model further emphasizes this by stating that the highest attainable charge carrier velocity is also inversely related to the effective mass [71]. Table 5 presents the calculated effective masses of electrons (m_e^*) and holes (m_h^*) for $TlGeCl_3$ and $TlSnCl_3$ at the *R*-point under varying pressures. These values are significantly lower than those in other lead free perovskites like $SrTiO_3$ ($m_e^* = 4.8\ m_0$ and $m_h^* = 9.8\ m_0$) [72], $MASnCl_3$ ($m_e^* = 1.94\ m_0$ and $m_h^* = 0.63\ m_0$) [73], $MASnBr_3$ ($m_e^* = 5.88\ m_0$ and $m_h^* = 0.65\ m_0$) [73], and $MASnI_3$ ($m_e^* = 3.74\ m_0$ and $m_h^* = 0.59\ m_0$) [73]. They are also lower than double

Table 5
Pressure-dependent effective masses of electrons (m_e^*) and holes (m_h^*) at the *R*-symmetry point in the conduction band (CB) and valence band (VB) for $TlGeCl_3$ and $TlSnCl_3$.

Compounds	Effective mass	0 GPa	1 GPa	2 GPa	3 GPa	4 GPa	5 GPa	6 GPa	6.5 GPa
$TlGeCl_3$	m_e^*/m_0	0.133	0.162	0.168	0.143	0.141	0.139	0.174	0.164
	m_h^*/m_0	0.034	0.023	0.186	0.126	0.009	0.006	0.003	0.004
	m_h^*/m_e^*	0.251	0.142	1.107	0.881	0.064	0.043	0.017	0.024
$TlSnCl_3$	m_e^*/m_0	0.266	0.191	0.161	0.154	0.192	0.158	0.172	0.144
	m_h^*/m_0	0.037	0.031	0.023	0.018	0.013	0.009	0.006	0.005
	m_h^*/m_e^*	0.140	0.162	0.143	0.117	0.068	0.057	0.035	0.034

perovskites like $Cs_2AgAsCl_6$ ($m_e^* = 0.62\ m_0$ and $m_h^* = 0.47\ m_0$) [69] and $Cs_2AuScBr_6$ ($m_e^* = 0.28\ m_0$ and $m_h^* = 0.14\ m_0$) [74]. Furthermore, $TlMCl_3$ (M = Ge, Sn) shows much smaller effective masses than common inorganic semiconductors like silicon ($m_e^* = 0.96\ m_0$ and $m_h^* = 0.26\ m_0$), BN ($m_e^* = 0.94\ m_0$ and $m_h^* = 0.53\ m_0$), AlN ($m_e^* = 0.53\ m_0$ and $m_h^* = 1.44\ m_0$) and GaN ($m_e^* = 0.14\ m_0$ and $m_h^* = 0.86\ m_0$) at ambient pressure [75]. The significantly lower effective masses of electrons (m_e^*) and holes (m_h^*) in $TlGeCl_3$ and $TlSnCl_3$ compared to other halide perovskites and well-known inorganic semiconductors indicates their importance in electronic applications.

These low effective masses highlight into superior charge transport properties. For example, $TlGeCl_3$ exhibits an electron effective mass as low as 0.133 m_0 at 0 GPa, with the hole effective mass dropping to a remarkable 0.004 m_0 under higher pressures. $TlSnCl_3$ shows similarly impressive values, with m_e^* decreasing to 0.144 m_0 and m_h^* reaching an ultra-low 0.005 m_0 at 6.5 GPa. The remarkable electron transport properties of both $TlGeCl_3$ and $TlSnCl_3$ position them as highly promising candidates for use in solar technologies. Their lower effective masses allow for faster charge carrier movement, leading to enhanced carrier mobility, which is essential for high-efficiency solar cells. These properties make $TlMCl_3$ (M = Ge, Sn) ideal for photovoltaic applications, offering the potential for more efficient energy conversion in solar devices.

Furthermore, the ratio of hole-to-electron effective masses (m_h^*/m_e^*) provides intriguing insights into the behavior of these materials. In $TlGeCl_3$, this ratio fluctuates more dramatically, indicating a greater sensitivity of its band structure to pressure variations, particularly within the valence band. In contrast, $TlSnCl_3$ exhibits a steady decline in this ratio, suggesting a more stable and predictable response to pressure changes, especially in its conduction band.

To gain deeper insights into how external pressure influences the electronic structures, we calculated the partial density of states (PDOS) for $TlMCl_3$ (M = Ge, Sn) under varying pressures ranging from 0 to 6.5 GPa. The resulting PDOS plots for $TlGeCl_3$ and $TlSnCl_3$, illustrated in Fig. 9(a-d) and **10(a–d)**, reveal the intricate changes in electronic states as pressure is applied. The vertical dashed line at 0 eV marks the Fermi energy (E_F), serving as a reference point for the electronic states in the system. The pressure-induced reduction of the band gap (E_g) is evident in the PDOS diagrams, where the valence and/or conduction bands shift towards the Fermi level (E_F). As pressure increases from 0 to 6.5 GPa, enhanced hybridization between Tl-6*p* and Ge-4*p* or Cl-3*p* orbitals in $TlGeCl_3$, drives the conduction bands downward, reducing the band gap. A similar trend is observed in $TlSnCl_3$, with interactions between Tl-6*p*, Sn-5*p*, and Cl-3*p* orbitals pushing the conduction bands closer to E_F. The pressure-induced shortening of Tl–Cl and Ge/Sn–Cl bond lengths (see Table 1) strengthens hybridization, especially near the conduction band minimum (CBM) at the *R*-point of the Brillouin zone. This effect closes the band gap, leading to a transition to metallic behavior. Notably, the valence bands remain stable, emphasizing the pivotal role of the conduction band in this transition. This behavior, fully supported by the **band diagrams**, underscores the significant impact of external pressure on the electronic structure.

In $TlGeCl_3$, as depicted in Fig. 9(a-d), the valence bands are shaped by the interplay of Tl-6*s* and Cl-3*p* orbitals, with a subtle yet significant contribution from Ge-4*s* electrons. The conduction bands, on the other hand, are primarily dominated by Tl-6*p* and Ge-4*p* orbitals, with a lesser but noticeable influence from Cl-3*p* orbitals. Similarly, in $TlSnCl_3$ (see Fig. 10(a-d)), the valence bands arise from the hybridization of Tl-6*s* and Cl-3*p* orbitals, complemented by a minor input from Sn-5*s* electrons. The conduction bands here are chiefly governed by Tl-6*p* and Sn-5*p* orbitals, with Cl-3*p* orbitals playing a supportive role. In both $TlGeCl_3$ and $TlSnCl_3$, the Tl-6*p* state plays the most prominent role in the conduction bands, contributing significantly to the total density of states (DOS). This characteristic aligns with the behavior seen in other thallium-based lead-free perovskites, such as $TlGeCl_xBr_{3-x}$ (x = 0, 1, 2, 3) [36], $TlBF_3$ [65], $TlBX_3$ (B = Ge, Sn; X = Cl, Br, I) [32], $TlLF_3$ (L = Ca, Cd) [76], $TlAF_3$ (A = Ge, Sn, Pb) [77], $TlXF_3$ (X = Ca, Cd, Hg, and Mg) [78], and $XBaF_3$ (X = Al and Tl) [79]. For both $TlGeCl_3$ and $TlSnCl_3$ under pressure, as depicted in Fig. 9(a-d) and **10(a–d)**, a significant shift occurs in the partial density of states (PDOS), particularly in the peaks of the Cl-3*p* orbitals in the valence band and the Tl-6*p* orbitals in the conduction band near the Fermi level. These peaks, highlighted by dashed ellipses in the figures, diminish in intensity as pressure increases, which in turn amplifies the difference between the nearest peak values of the Cl-3*p* orbitals in the valence band and the Tl-6*p* orbitals in the conduction band around the Fermi level. This clear modification in the electronic structure indicates that the properties of $TlMCl_3$ (M = Ge, Sn) can be effectively tuned through the application of external hydrostatic pressure.

3.3. Effect of spin-orbit coupling (SOC) on the band structure

To investigate the influence of spin-orbit coupling (SOC) on the electronic properties of $TlMCl_3$ (M = Ge, Sn) perovskites at ambient pressure for the first time, we incorporated the SOC Hamiltonian into our calculations [80]:

$$H_{SOC} = \frac{\hbar}{4m_0c^2}\left(\vec{F} \times \vec{P}\right).\vec{s} \tag{5}$$

In this equation, H_{SOC} represents the SOC Hamiltonian, where $\hbar$ is the reduced Planck's constant, $\vec{P}$ is the orbital angular momentum, $\vec{F}$ is the potential energy or force, m_0 is the mass of a free electron, and $\vec{s}$ is the spin angular momentum. SOC arises due to the interaction between the electron's spin and its orbital motion, becoming particularly significant in materials containing heavy atoms.

To accurately capture the relativistic effects, we employed the GGA-PBE + SOC functional method at ambient pressure. This allowed us to evaluate how the heavy atoms Tl and Ge/Sn influence the electronic structure of $TlMCl_3$ (M = Ge, Sn) when SOC is included. Due to the large atomic number (*Z*) of Tl (81), SOC has a strong impact on the electronic and spin properties of these perovskites. Such strong SOC effects are crucial in $TlGeCl_3$ and $TlSnCl_3$, making them suitable candidates for advanced optoelectronic and spintronic applications. The resulting band structures are presented in Fig. 8(a-d), demonstrating significant effects of SOC, particularly in the conduction band regions. As illustrated in Fig. 8(a-d), the most prominent impact of SOC is the downward shift of the

conduction band minimum (CBM), while the valence band maximum (VBM) remains largely unaffected. In $TlMCl_3$ (M = Ge, Sn) perovskites, the CBM is primarily composed of Tl-6*p* and Ge/Sn-4*p*/5*p* orbitals, which are highly susceptible to SOC due to the heavy atomic masses of Tl and Ge/Sn. SOC introduces a splitting and lowering of the energy levels in these *p*-orbitals, leading to the observed downward shift of the CBM. This shift reduces the overall bandgap by decreasing the energy difference between the CBM and VBM. The conduction band, influenced by the heavy atoms involved, shows significant sensitivity to SOC effects. In contrast, the VBM is dominated by the lighter Cl-3*p* orbitals, which are far less affected by relativistic SOC effects. As a result, the VBM remains nearly unchanged, with SOC exerting a minimal influence on its energy levels. In the case of $TlGeCl_3$ and $TlSnCl_3$, the inclusion of SOC reduces the bandgap to 0.66 eV and 0.57 eV, respectively, as depicted in Fig. 8(b–d). These results align well with previous studies on heavy-element compounds, where SOC typically induces similar downward shifts in the conduction band without significantly altering the VBM [81,82].

These findings, as explored for the first time in this study, offer critical insights into the potential of these materials for cutting-edge device applications, particularly in optoelectronics and spintronics. Our work provides a theoretical foundation that can guide future experimental efforts in harnessing the unique properties of $TlMCl_3$ (M = Ge, Sn) perovskites for advanced technological applications.

3.4. Optical properties

Optical characteristics are a direct reflection of a material's electronic properties, offering insight into how it interacts with incident light. Leveraging pressure as a simple yet an effective approach can significantly enhance the efficiency of $TlMCl_3$ (M = Ge, Sn) in solar cells and other optoelectronic devices. In our study, we thoroughly examined the key optical properties of cubic $TlMCl_3$ (M = Ge, Sn) perovskites under varying hydrostatic pressures, ranging from 0 to 6.5 GPa, and across a photon energy spectrum of 0–10 eV. Our analysis involved calculating the real and imaginary parts of the dielectric function, along with refractive index, reflectivity, absorption, and optical conductivity, utilizing the WIEN2k code. To quantify additional optical characteristics, the dielectric function, defined as $\varepsilon(\omega) = \varepsilon_1(\omega) + i\varepsilon_2(\omega)$, must be computed, where $\varepsilon_1(\omega)$ and $\varepsilon_2(\omega)$ are the real and imaginary parts, respectively. For cubic crystals, the dielectric function is isotropic, simplifying optical computations by considering field polarization along [001] direction. However, $\varepsilon_1(\omega)$ is derived from the Kramers-Kronig relation [83,84], while $\varepsilon_2(\omega)$ is computed using momentum tensors of wave functions, with energy conservation enforced by the δ function. Other optical properties are derived from established formulas [85].

The real part of the dielectric function, $\varepsilon_1(\omega)$, for $TlGeCl_3$ and $TlSnCl_3$ under varying pressures is presented in Fig. 11(a). Initially, $\varepsilon_1(\omega)$ decreases sharply until reaching a minimum, followed by a rise. The static dielectric constants $\varepsilon_1(0)$, listed in Table 6, are crucial for determining charge recombination rates, directly affecting the efficiency of optoelectronic devices. Notably, the computed $\varepsilon_1(0)$ values at zero pressure align closely with previous DFT findings for other Tl-based halide perovskites, affirming the precision and reliability of our calculations [77,86,87]. Higher $\varepsilon_1(0)$ values indicate reduced recombination rates and improved device performance. Pressure application increases $\varepsilon_1(0)$ compared to unpressurized conditions, potentially enhancing optoelectronic effectiveness by reducing carrier recombination. This enhancement correlates with the smaller band gaps observed under pressure. Under ambient conditions, both compounds exhibit similar $\varepsilon_1(\omega)$ trends, with a decrease in the visible region and a sharp increase in the ultraviolet region, turning negative around 7 eV, indicating a transition from dielectric to metallic behaviour. The increased $\varepsilon_1(0)$ at 6.5 GPa reflects the potential for improved optoelectronic efficiency under pressure, highlighting these compounds' relevance in microelectronic applications due to their high dielectric constants. Moreover, Ge-based halide perovskites exhibit slightly greater dielectric behaviour than Sn-based halides due to Ge's smaller atomic radius and higher electronegativity, leading to stronger bonding with halide ions.

The imaginary component of the dielectric function, $\varepsilon_2(\omega)$, plays a crucial role in understanding the band gap-dependent absorption behavior of materials, as it governs interband transitions within the device's material. However, $\varepsilon_2(\omega)$ represents the sum of all transitions from the valence to conduction bands, dictating the maximum absorption area. The pressure-affected $\varepsilon_2(\omega)$ for $TlGeCl_3$ and

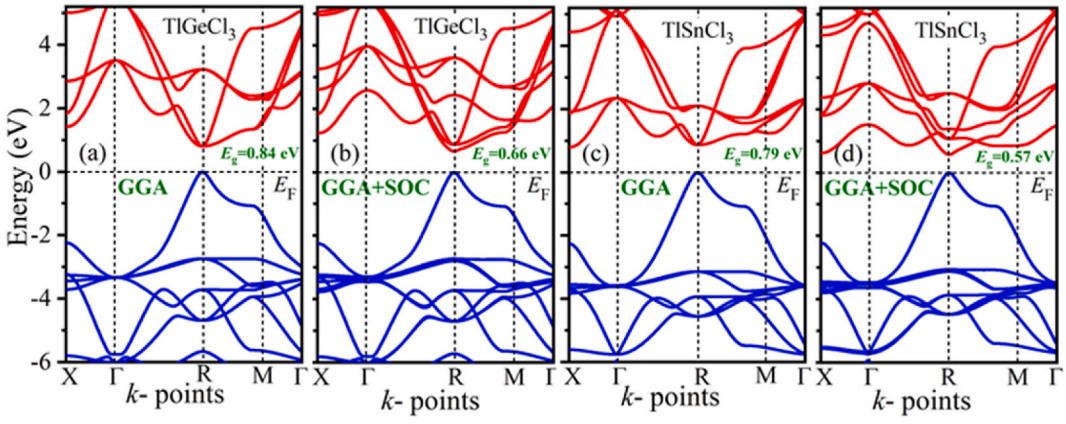

Fig. 8. (a, c) The electronic band structure of $TlMCl_3$ (M = Ge, Sn) without SOC, and (b, d) with SOC included, revealing how SOC modifies the band gap and conduction bands.

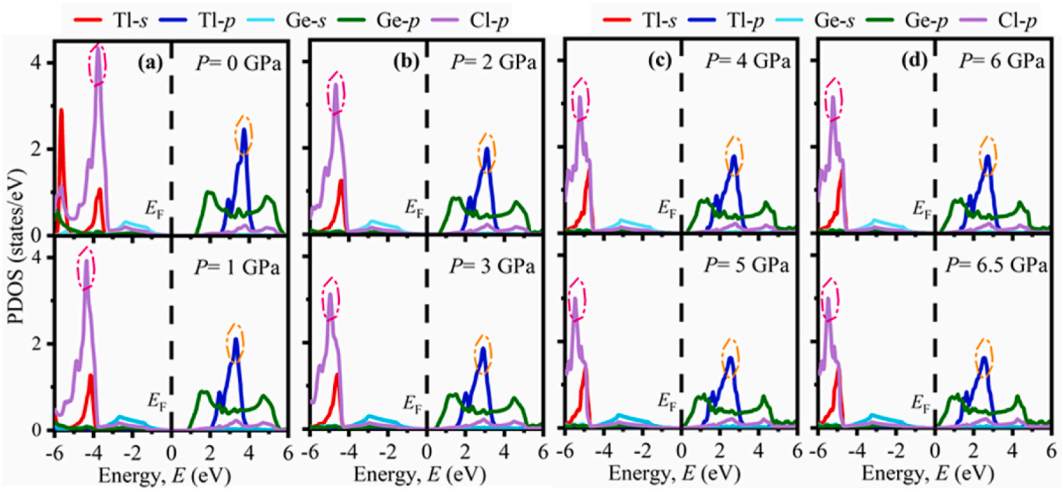

Fig. 9. Analysis of the partial density of states (PDOS) for $TlGeCl_3$ at various pressures.

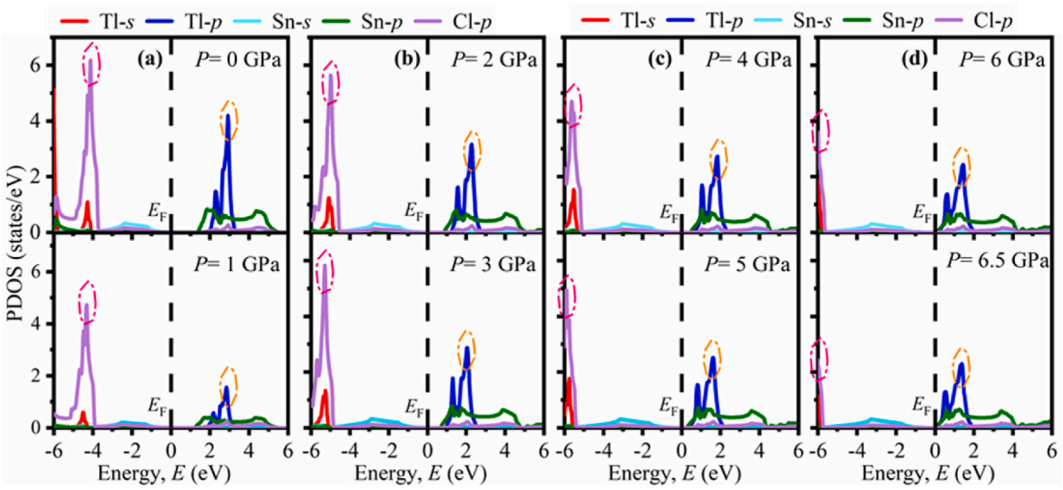

Fig. 10. Analysis of the partial density of states (PDOS) for $TlSnCl_3$ at various pressures.

$TlSnCl_3$ is shown in Fig. 11(b), where increased pressure leads to a rise in the dielectric constant's peak in the visible to ultraviolet regions. The maximum value of $\varepsilon_2(\omega)$, known as the first absorption peak (FAP), represents the point where the material exhibits the strongest absorption of light. The FAP of $TlGeCl_3$ and $TlSnCl_3$ is around 2.4 eV under pressure, signifies effective light absorption in visible spectrum, boosting their performance in optoelectronic devices like solar cells and LEDs. These peaks result from electron transitions from the Cl-3*p* state in the valence band to the Tl-6*p* and Ge/Sn-3*d*/4*d* states in the conduction band at the *R* symmetry point (see Figs. 9 and 10). Notably, the optical response structures shift toward higher energy as the cation changes from Ge to Sn, reflecting the second valence band's shift away from the Fermi level.

Fig. 11(c) shows the refractive index calculations under pressures up to 6.5 GPa. The static refractive index $n(0)$ for both compounds, presented in Table 6, follows the relation [88] $n(0)^2 \approx \varepsilon_1(0)$, confirming the accuracy of our calculations. At ambient pressure, the static refractive index of $TlGeCl_3$ is 2.16, aligning well with previous theoretical results [34]. The $n(\omega)$ spectrum displays similar features to the $\varepsilon_1(\omega)$ spectrum (see Fig. 11(a)). A high refractive index $n(0)$ significantly slows down incident photons as they interact with electrons, enhancing the photon-electron interaction and thereby increasing photocurrent production, which improves solar cell efficiency. Additionally, the increase in $n(0)$ under pressure suggests potential applications of these perovskites in photonic crystals, QLED, OLED, solar panel and waveguides. Optoelectronic activities, such as those in solar cells and LEDs, typically require materials with a refractive index $n(\omega)$ between 2.0 and 4.0 for optimal performance [89]. The studied materials exhibit $n(\omega)$ values between 2.0 and 4.0 under pressure, suitable for optoelectronic applications. A refractive index greater than 1 confirms their semiconducting nature and indicates strong covalent bonding rather than ionic [90].

Fig. 12(a) illustrates the reflectivity spectra $R(\omega)$ of $TlMCl_3$ (M = Ge, Sn), which result from the contribution between the Cl-3*p* states in the valence band and the Tl-6*p* as well as Ge/Sn-3*d*/4*d* states in the conduction band. The static reflectivity of the studied

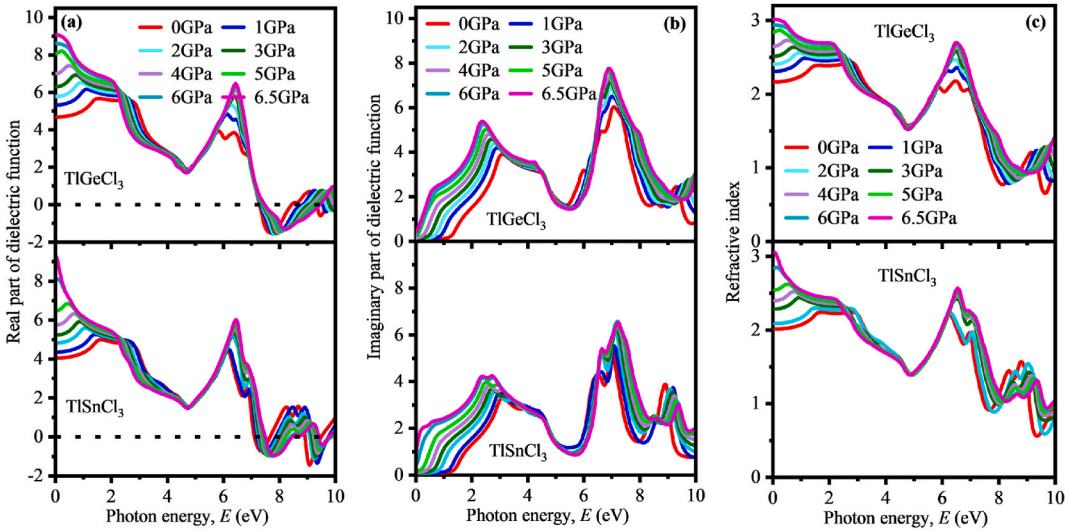

Fig. 11. The effect of applied pressure on (a) the real part, (b) the imaginary part of the dielectric function, and (c) the refractive index of $TlMCl_3$ (M = Ge, Sn).

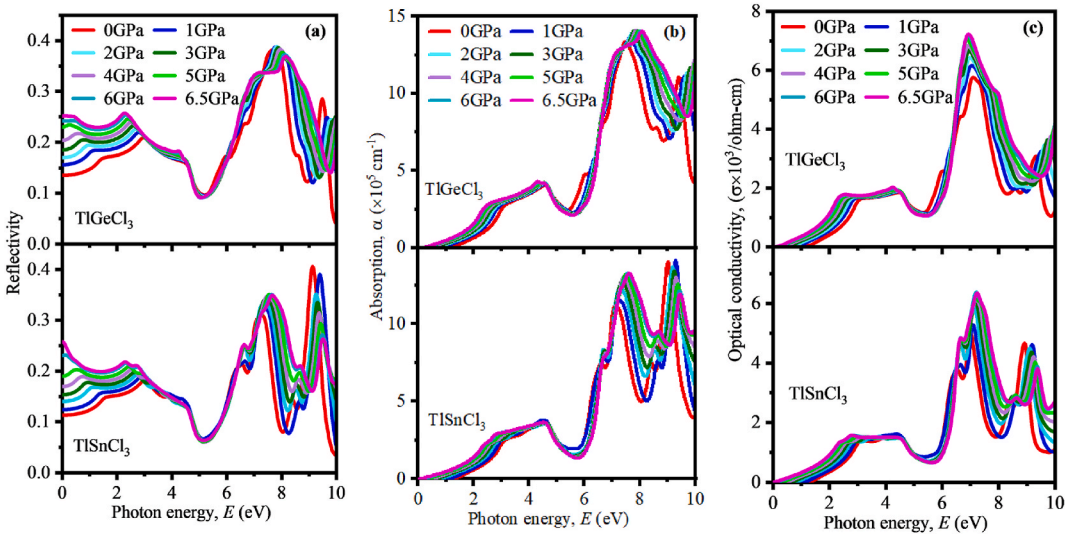

Fig. 12. The effect of applied pressure on (a) reflectivity, (b) absorption, and (c) optical conductivity of $TlMCl_3$ (M = Ge, Sn).

Table 6
Analysis of the optical constants of $TlMCl_3$ (M = Ge, Sn) under various applied pressures.

Compounds	Optical constant	0 GPa	1 GPa	2 GPa	3 GPa	4 GPa	5 GPa	6 GPa	6.5 GPa
$TlGeCl_3$	$\varepsilon_1(0)$	4.68	5.32	5.77	6.31	7.0	8.07	8.61	9.07
	$n(0)$	2.16	2.31	2.40	2.51	2.65	2.84	2.94	3.01
	$R(0)$	13.5 %	15.6 %	17 %	18.5 %	20.4 %	23 %	24.2 %	25.2 %
$TlSnCl_3$	$\varepsilon_1(0)$	4.05	4.36	4.83	5.23	5.75	6.47	8.09	9.29
	$n(0)$	2.01	2.09	2.20	2.29	2.40	2.54	2.84	3.05
	$R(0)$	11.3 %	12.4 %	14 %	15.3 %	16.9 %	19 %	23.1 %	25.8 %

compounds is below 15 % at zero pressure, indicating their effectiveness in absorbing incoming light across energy values from zero to the band gap in the infrared radiation (IR) region. The zero-frequency reflectivity $R(0)$ of $TlMCl_3$ (M = Ge, Sn) increases under hydrostatic pressure, which could potentially reduce solar cell efficiency. The reflectivity $R(\omega)$ of $TlGeCl_3$ and $TlSnCl_3$ is below 10 % in the 4.91–5.35 eV and 4.80–5.75 eV ranges, respectively, making them highly transparent in the infrared, visible, and low-frequency

UV regions. This transparency makes them ideal for lenses and anti-reflection coatings in optical applications. The reflectivity peaks reach a maximum value of 39 % at ~ 7.9 eV for $TlGeCl_3$ and 40 % at ~ 8.8 eV for $TlSnCl_3$ in the UV range highlight their effectiveness at reflecting UV light. This property is beneficial for applications such as UV protective coatings, optical filters, and reflective mirrors in UV spectroscopy. Additionally, these materials can be used in solar energy applications to reflect harmful UV rays, improving the durability of solar panels.

The optical absorption coefficient quantifies the energy absorbed per unit length, providing insight into the material's efficiency in solar energy utilization. Fig. 12(b) presents the absorption coefficient (α) of $TlMCl_3$ (M = Ge, Sn) under pressure. Notably, similar absorption features are observed in other cubic halide perovskites at ambient pressure [25,26,28,29], underscoring a consistent optical behavior across these materials. Fig. 12(b) shows that the absorption (α) of $TlGeCl_3$ and $TlSnCl_3$ begins above 0 eV due to their band gaps at ambient pressure, with similar peaks in the infrared-to-visible range and a rising trend towards the ultraviolet. Under increased pressure from 0 to 6.5 GPa, the absorption peaks remain similar in the ultraviolet region, though the spectra broaden and shift to lower energies due to a reduced band gap. This shift enhances the materials' effectiveness for applications like solar cells, as it improves absorption across various energy ranges. Additionally, the higher absorption in the ultraviolet region suggests potential uses in UV detectors, anti-reflective coatings, and other technologies. The ability to absorb ultraviolet light efficiently makes these materials ideal for applications in surgical device manufacturing, where sterilization becomes easier and more efficient. The rise in absorption spectra is primarily attributed to localized interband transitions, which elevate the Bloch character of electronic states, amplifying the local field and enhancing dielectric properties under pressure [28]. A similar behavior has been observed in compounds like $CsSnBr_3$ [28], $CsSnCl_3$ [26] and $PbSnO_3$ [91] underscoring the broad applicability of pressure-tuned halide perovskites in cutting-edge optoelectronic and medical applications.

Optical conductivity also known as photoconductivity, increases with greater photon absorption, resulting in enhanced photoconductivity and electrical conductivity. Fig. 12(c) illustrates the optical conductivity (σ) of $TlGeCl_3$ and $TlSnCl_3$ across a pressure range of 0–6.5 GPa. The conductivity spectra align with the absorption spectra as shown in Fig. 12(b), where enhanced photon absorption drives increased conductivity through the release of free carriers. The optical conductivity rises with applied pressure, reflecting the enhanced absorption coefficient and correlating with the dielectric function peaks observed when the real part of the dielectric function becomes negative (see Fig. 11(a)). Under applied pressure, the conductivity increases significantly in the ultraviolet (UV) region, indicating that the materials become more conductive when exposed to UV light. This behavior makes these materials particularly effective for high-energy optoelectronic applications, such as UV detectors, high-performance solar cells, and other devices that require efficient energy absorption and conversion at high frequencies. The optical conductivity at lower energy levels is crucial for solar cells and other optoelectronic devices. Our calculations show that conductivity at ambient pressure is lower than at higher pressures. This indicates that the band gap decreases with pressure, leading to enhanced conductivity. At 6.5 GPa, the materials reach their highest conductivity, particularly in the visible region. This behavior is expected, as photoconductivity and electrical conductivity increase with absorbed photons. The optical conductivity describes the relationship between the induced current and the electric field of light, which strengthens as pressure rises. These findings are consistent with other lead-free perovskites like $CsGeCl_3$ [25], $CsGeBr_3$ [28], $CsSnCl_3$ [26], and $TlGeF_3$ [34]. The high conductivity, along with strong absorption and low reflectivity, makes $TlMCl_3$ (M = Ge, Sn) perovskites excellent candidates for optoelectronic and photovoltaic applications.

3.5. Elastic constants and mechanical properties

The mechanical stability of a material is essential for its practical applications, as it ensures that the material can withstand external forces and pressures. Elastic constants (C_{ij}) play a vital role in determining a material's mechanical properties, such as solidity,

Table 7
Comparative analysis of elastic constants C_{ij} (GPa) and Cauchy pressures (C_{12}-C_{44}) (GPa) for $TlMCl_3$ (M = Ge, Sn) across different hydrostatic pressures.

Pressure (GPa)	Compound	C_{11}	C_{12}	C_{44}	C_{12}-C_{44}	Remarks
0	$TlGeCl_3$	59.53	12.68	8.66	4.02	This work
	$TlSnCl_3$	53.66	8.91	3.54	5.37	
0	$TlGeCl_3$	57.94	12.50	8.05	4.45	Ref [32]
	$TlSnCl_3$	51.35	8.94	3.40	5.54	
1	$TlGeCl_3$	68.20	14.20	8.94	5.26	
	$TlSnCl_3$	63.51	9.84	3.15	6.69	
2	$TlGeCl_3$	76.40	15.35	9.25	6.1	
	$TlSnCl_3$	72.54	11.69	2.77	8.92	
3	$TlGeCl_3$	84.37	16.65	9.52	7.13	
	$TlSnCl_3$	81.96	13.17	2.42	10.75	
4	$TlGeCl_3$	93.49	19.04	9.88	9.16	
	$TlSnCl_3$	90.42	14.26	1.97	12.29	
5	$TlGeCl_3$	99.86	19.19	10.14	9.05	
	$TlSnCl_3$	99.52	16.10	1.75	14.35	
6	$TlGeCl_3$	108.56	21.65	10.48	11.17	
	$TlSnCl_3$	107.24	17.12	1.36	15.76	
6.5	$TlGeCl_3$	112.14	22.25	10.64	11.61	
	$TlSnCl_3$	111.43	17.30	1.34	16.04	

stiffness, brittleness, malleability, and elastic anisotropy. These constants are critical for selecting materials for engineering purposes because they describe the material's response to stress and its ability to resist deformation under pressure. To evaluate the mechanical stability of $TlMCl_3$ (M = Ge, Sn), the elastic constants were calculated at both ambient and applied pressures. The results, presented in Table 7 and plotted in Fig. 14(a and b), were obtained using the stress-strain approach within the GGA-PBE method. For a cubic structure, the relevant elastic constants are C_{11}, C_{12} and C_{44}, representing longitudinal stiffness, off-diagonal stiffness, and shear stiffness, respectively. The calculated elastic constants meet the Born stability criteria [92], which are:

$$C_{11} + 2C_{12} > 0,\ C_{44} > 0, \text{ and } C_{11}–C_{12} > 0 \tag{6}$$

These criteria ensure that both compounds remain mechanically stable under applied pressure. Fig. 14(a and b) illustrate the pressure dependence of the elastic constants for $TlGeCl_3$ and $TlSnCl_3$, respectively. Furthermore, the computed elastic constants and other mechanical properties at zero pressure show excellent agreement with previous DFT results for other halide perovskites, reflecting the accuracy and reliability of our calculations [26,93]. For $TlGeCl_3$, the linear increase in C_{11} and C_{12}, along with the gradual rise in C_{44} observed in Fig. 14(a), reflects enhanced stiffness and structural integrity, making this material well-suited for applications requiring stability under compression. In contrast, $TlSnCl_3$, as depicted in Fig. 14(b), exhibits a slight decrease in C_{44} despite the linear increase in C_{11} and C_{12}, indicating reduced shear resistance. This reduction suggests greater machinability, positioning $TlSnCl_3$ as an ideal choice for applications that require ease of shaping and forming under pressure. These contrasting elastic behaviours underscore the materials' suitability for different engineering applications, each driven by their unique response to pressure. The data from Table 7 also reveal that as pressure increases from 0 to 6.5 GPa, the elastic constant C_{11}, C_{12}, and C_{44} increase by 88 %, 76 %, and 23 %, respectively, indicating a substantial enhancement in overall stiffness for $TlGeCl_3$ perovskite. In $TlSnCl_3$, the elastic constant C_{11}, C_{12} show even more pronounced increases of 108 % and 94 %, respectively, while C_{44} exhibits a notable 62 % decrease. This stark contrast underscores the greater sensitivity of the longitudinal stiffness constant C_{11} to applied pressure compared to the other elastic constants, highlighting the distinctive mechanical responses of these materials under pressure.

The mechanical properties of $TlMCl_3$ (M = Ge, Sn) have been thoroughly investigated by computing the Voigt and Reuss bulk moduli (B_V and B_R), shear moduli (G_V and G_R), Young's modulus (E), Poisson's ratio (ν), and elastic anisotropy (A). The computed values are presented in Table 8 and are determined using the following formulas [94,95]:

$$B_{V=}\frac{1}{3}(C_{11}+2C_{12}) \tag{7}$$

$$G_V=\frac{1}{5}(C_{11}-C_{12}+3C_{44}) \tag{8}$$

$$B_R=B_{V=}\frac{1}{3}(C_{11}+2C_{12}) \tag{9}$$

$$G_{R=}\frac{5C_{44}(C_{11-}C_{12})}{[4C_{44}+3(C_{11-}C_{12})]} \tag{10}$$

The overall bulk modulus (B) and shear modulus (G) are then calculated as the arithmetic mean of the Voigt and Reuss values, in accordance with Hill's theory [96]:

$$B=\frac{1}{2}(B_V+B_R) \tag{11}$$

$$G=\frac{1}{2}(G_V+G_R) \tag{12}$$

In addition, Young's modulus (E) and Poisson's ratio (ν) are determined using [97,98]:

$$E=\frac{9BG}{3B+G} \tag{13}$$

$$\nu=\frac{(3B-2G)}{2(3B+G)} \tag{14}$$

Table 8 shows the variations in these elastic moduli under different applied pressures and compares them with available published data, which are also illustrated in Fig. 15(a and b). As depicted in Fig. 15(a and b), the bulk modulus (B) for both compounds increase linearly with pressure, indicating enhanced resistance to external deformation and greater stiffness compared to their non-pressurized states, resulting from more closely packed atoms. The shear modulus (G) of $TlGeCl_3$ and $TlSnCl_3$ also increases linearly with pressure, signifying increased resistance to shear deformation and fracture. When comparing the bulk and shear moduli of $TlGeCl_3$ and $TlSnCl_3$ under pressure, $TlGeCl_3$ demonstrates better values for both B and G. This suggests that $TlGeCl_3$ is mechanically more robust under pressure. This aligns with the findings of Marjaoui et al. [34], who observed a similar increase in the elastic moduli of $TlGeCl_3$ with pressure up to 25 GPa, thereby supporting the validity of the current results. Therefore, this study reveals that applying hydrostatic pressure improves the hardness and mechanical robustness of $TlMCl_3$ (M = Ge, Sn) perovskites.

Table 8
Pressure-dependent mechanical parameters including bulk modulus B (GPa), shear modulus G (GPa), Young's modulus E (GPa), Pugh's ratio (B/G), Poisson's ratio (ν), machinability index (μ_M), and Zener anisotropy factor (A) for $TlMCl_3$ (M = Ge, Sn).

Pressure (GPa)	Compound	B	G	E	B/G	ν	μ_M	A	Remarks
0	$TlGeCl_3$	28.23	13.07	33.98	2.16	0.300	3.26	0.37	This work
	$TlSnCl_3$	23.83	8.21	22.08	2.90	0.346	6.73	0.16	
0	$TlGeCl_3$	27.64	12.39	32.33	2.23	0.305	3.43	0.35	Ref [32]
	$TlSnCl_3$	23.07	7.82	21.08	2.95	0.348	6.79	0.16	
1	$TlGeCl_3$	32.20	14.18	37.10	2.27	0.308	3.60	0.33	This work
	$TlSnCl_3$	27.73	8.74	23.74	3.17	0.357	8.80	0.12	
2	$TlGeCl_3$	35.70	15.29	40.14	2.34	0.313	3.86	0.30	
	$TlSnCl_3$	31.97	9.10	24.93	3.51	0.370	11.54	0.09	
3	$TlGeCl_3$	39.22	16.31	42.98	2.41	0.317	4.12	0.28	
	$TlSnCl_3$	36.10	9.54	26.29	3.78	0.379	14.92	0.07	
4	$TlGeCl_3$	43.86	17.41	46.12	2.52	0.325	4.44	0.27	
	$TlSnCl_3$	39.64	9.80	27.15	4.05	0.386	20.12	0.05	
5	$TlGeCl_3$	46.08	18.35	48.60	2.51	0.324	4.54	0.25	
	$TlSnCl_3$	43.91	10.29	28.63	4.27	0.391	25.09	0.04	
6	$TlGeCl_3$	50.62	19.36	51.52	2.62	0.330	4.83	0.24	
	$TlSnCl_3$	47.48	10.37	28.99	4.58	0.398	34.91	0.03	
6.5	$TlGeCl_3$	52.21	19.84	52.82	2.63	0.331	4.91	0.24	
	$TlSnCl_3$	48.68	10.91	30.46	4.46	0.396	35.88	0.03	

Moreover, this study investigates the mechanical behavior of $TlMCl_3$ (M = Ge, Sn) under varying pressures, with a particular focus on Poisson's ratio (ν), Pugh's ratio (B/G), Cauchy pressure ($C_{12} - C_{44}$), machinability index (μ_M), and elastic anisotropy (A). Both ν and B/G are indicators of ductility. The findings are summarized in Table 8 and illustrated in Fig. 13(a and b). A material is considered ductile if $\nu > 0.26$ and $B/G > 1.75$, otherwise brittleness [99,100]. The data shows that both $TlGeCl_3$ and $TlSnCl_3$ are ductile, and their ductility increases with pressure, as indicated by the rising values of ν and B/G (see Fig. 13(a and b)). Cauchy pressure is also used to determine brittleness or ductility [101]. Positive values indicate ductility, while negative values indicate brittleness. The computed $(C_{12} - C_{44})$ values for both compounds are positive under all applied pressures, confirming their ductility. The increasing positive values with pressure indicate enhanced ductility, with $TlSnCl_3$ showing slightly higher ductility than $TlGeCl_3$ (see Table 8). The brittleness of semiconductor materials often limits their use, as it can lead to performance degradation and failures. In contrast, high ductility is essential for creating deformable, flexible, and robust electronics [102]. Pressure-enhanced ductility in $TlMCl_3$ (M = Ge, Sn) makes it more suitable for advanced applications such as flexible electronics, wearable devices, and robust solar cells.

The machinability index [99] ($\mu_m = \frac{B}{C_{44}}$) assesses the ease of shaping materials, with higher values indicating better machinability. The machinability of both compounds improves significantly under pressure (see Table 8). For $TlSnCl_3$, in particular, shows a dramatic increase in machinability index, approximately seven times higher at 6.5 GPa compared to $TlGeCl_3$, making it highly useful in industrial applications. Elastic anisotropy (A) is calculated using the Zener equation [103] ($(A = \frac{2C_{44}}{C_{11}-C_{12}})$). When A equals 1, it indicates isotropy; values differing from 1 suggest anisotropy [103]. According to Table 8, the values of A decrease from unity under hydrostatic pressure, implying that $TlGeCl_3$ and $TlSnCl_3$ become more anisotropic as pressure increases. This increased anisotropy suggests that the materials exhibit different mechanical properties in different directions under pressure.

The analysis of mechanical properties under pressure reveals that $TlMCl_3$ (M = Ge, Sn) perovskites exhibit increased ductility, improved machinability, and greater anisotropy with increasing pressure. $TlSnCl_3$, in particular, stands out with its higher ductility and machinability index, making it a promising candidate for industrial applications requiring high ductility and ease of shaping.

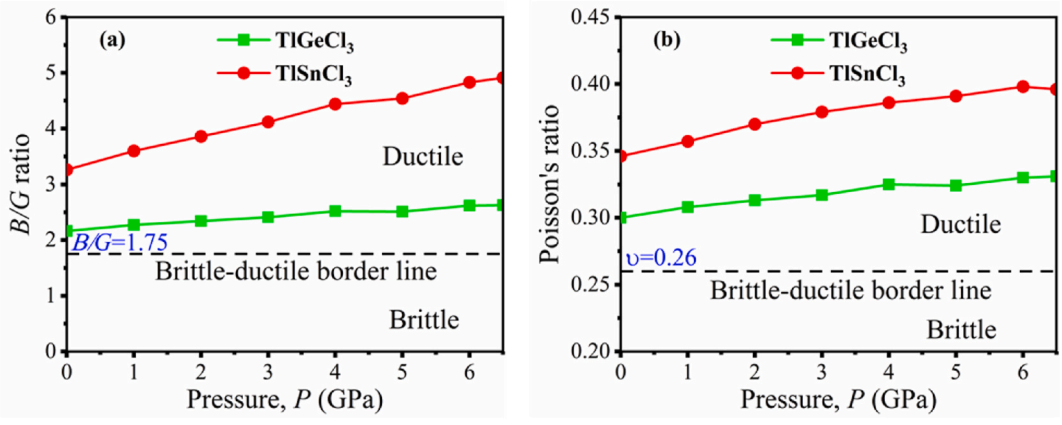

Fig. 13. Pressure-induced variations in (a) Pugh's ratio and (b) Poisson's ratio for $TlMCl_3$ (M = Ge, Sn).

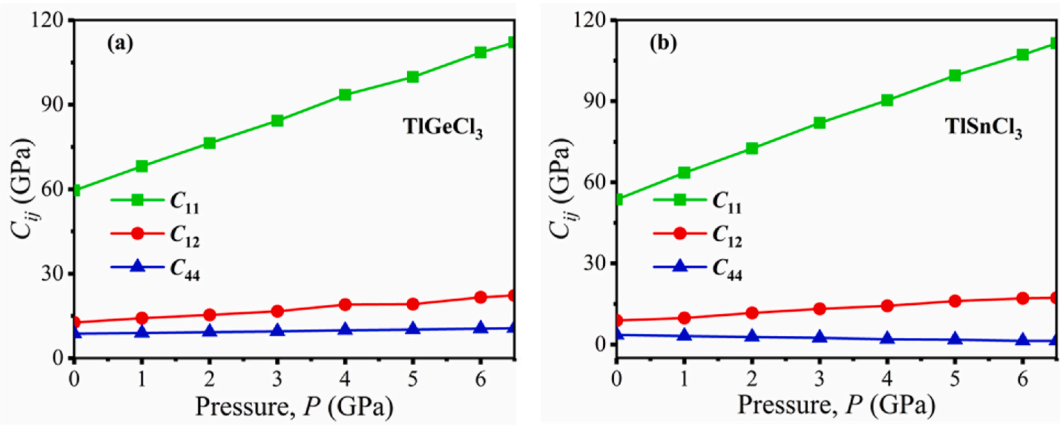

Fig. 14. The effect of pressure on the elastic constants for (a) $TlGeCl_3$ and (b) $TlSnCl_3$.

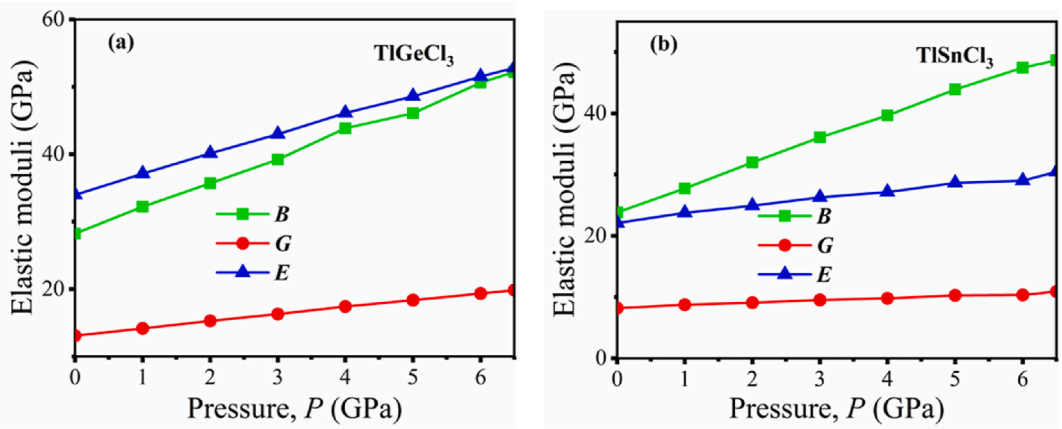

Fig. 15. The effect of pressure on the elastic moduli for (a) $TlGeCl_3$ and (b) $TlSnCl_3$.

3.6. *Thermodynamic properties*

The thermodynamic properties of $TlMCl_3$ (M = Ge, Sn) perovskites, such as Debye temperature (θ_D), melting temperature (T_m), and minimum thermal conductivity (k_{min}), have been calculated to investigate their behavior under pressure. The formulas and methodology for these calculations are detailed in the corresponding reference [104]. Our calculations, as shown in Table 9, reveal that θ_D, T_m, and k_{min} increase with pressure, indicating enhanced dynamical stability and hardness of these materials [104]. The increase in Debye temperature under pressure can be attributed to the strengthening of elastic wave velocities as binding forces intensify (refer to Table 9). Conversely, as temperature rises, θ_D decreases due to structural expansion, which lengthens the vibrational wavelengths of anions and cations, thus reducing vibrational frequencies (refer to Fig. 16(a and b)). Despite the absence of experimental or theoretical data for comparison, our results highlight the promising thermodynamic performance of $TlMCl_3$ (M = Ge, Sn) perovskites. Notably, the lower θ_D values for $TlGeCl_3$ and $TlSnCl_3$ at ambient pressure compared to materials like $MgSiO_3$ (θ_D = 984 K) [105], $KCaF_3$ (θ_D = 431 K) [106], $BaLiCl_3$ (θ_D = 285.4 K), and $BaNaCl_3$ (θ_D = 431 K) [107] suggest a softer lattice, which may have implications for their thermal properties. Interestingly, Debye temperature is intrinsically linked to lattice thermal conductivity, making it a key factor in

Table 9
Pressure-dependent thermodynamic properties for $TlGeCl_3$ and $TlSnCl_3$.

Compounds	Properties	0 GPa	1 GPa	2 GPa	3 GPa	4 GPa	5 GPa	6 GPa	6.5 GPa
$TlGeCl_3$	θ_D	155	199	206	212	218	222	228	230
	T_m	905	956	1005	1052	1106	1143	1195	1216
	k_{min}	0.234	0.305	0.318	0.330	0.342	0.352	0.363	0.368
$TlSnCl_3$	θ_D	145	149	151	154	156	159	160	164
	T_m	857	928	982	1037	1087	1141	1187	1212
	k_{min}	0.207	0.215	0.221	0.228	0.232	0.239	0.241	0.247

evaluating the thermoelectric potential of a material. While the θ_D values for $TlMCl_3$ (M = Ge, Sn) compounds are comparable to other perovskite like $CsOsCl_3$ and $CsOsBr_3$, their lower thermal conductivity could favor applications in thermoelectric devices, where efficient heat management is critical.

From Table 9, it is observed that both the melting temperature ($\boldsymbol{T_m}$) and minimum thermal conductivity ($\boldsymbol{k_{min}}$) increase with applied pressure. In $TlGeCl_3$, $\boldsymbol{T_m}$ ascends from 905 K at 0 GPa to an impressive 1216 K at 6.5 GPa, while in $TlSnCl_3$, $\boldsymbol{T_m}$ climbs from 857 K to 1212 K over the same pressure range. This trend is mirrored in the thermal conductivity, where $TlGeCl_3$'s $\boldsymbol{k_{min}}$ rises from 0.234 W/m·K to 0.368 W/m·K, and $TlSnCl_3$ sees a boost from 0.207 W/m·K to 0.247 W/m·K. This correlation is driven by the fact that higher melting temperatures signal stronger atomic bonds, which, in turn, facilitate better phonon propagation and enhance thermal conductivity. As pressure strengthens the material's resistance to melting, it simultaneously boosts its capacity to conduct heat efficiently. Thus, pressure not only enhances thermal stability but also improves heat transport, making these perovskites excellent candidates for high-temperature, high-pressure applications.

4. Conclusions

In this study, we explored the structural, electronic, optical, and mechanical properties of cubic $TlMCl_3$ (M = Ge, Sn) perovskite halides under hydrostatic pressure using DFT-based CASTEP simulations. The pressure range of 0–6.5 GPa was specifically selected because it captures the transition point where $TlMCl_3$ (M = Ge, Sn) shifts from a semiconductor to a metallic state. By thoroughly examining this phase transition, we unveil novel insights into how pressure influences the optoelectronic behavior—such as band gap closure, enhanced optical absorption, and pressure-induced improvements in mechanical properties of these materials. Our findings reveal that increasing pressure leads to a reduction in lattice constants and unit cell volumes, accompanied by enhanced elastic moduli, which contribute to their increased hardness. The analysis of Cauchy pressure, Poisson's ratio and Pugh's ratio indicates that $TlMCl_3$ (M = Ge, Sn) materials become more ductile under pressure, making them suitable for applications requiring high ductility. The increased ductility of $TlMCl_3$ (M = Ge, Sn) under pressure makes it a suitable material for cutting-edge technologies like flexible electronics, durable solar cells, and next-generation wearable devices. Electronic analyses demonstrate that pressure induces a semiconductor-to-metal transition, with the band gaps of $TlGeCl_3$ and $TlSnCl_3$ collapsing to 0 eV at specific pressures (6 GPa for $TlGeCl_3$ and 6.5 GPa $TlSnCl_3$ according to TB-mbj), as confirmed by partial density of states and band structure calculations. These transitions, alongside enhanced dielectric constants and refractive indices under pressure, suggest that $TlGeCl_3$ and $TlSnCl_3$ could significantly improve the efficiency of solar cells and LEDs by reducing carrier recombination and strengthening photon-electron interactions. Both $TlGeCl_3$ and $TlSnCl_3$ stand out with impressively low effective masses for both electrons and holes, far surpassing other halide perovskites and inorganic semiconductors. These lightweight charge carriers lead to excellent transport properties, making these materials ideal for high-performance solar technologies. With their ability to enhance charge mobility and energy conversion efficiency, $TlMCl_3$ (M = Ge, Sn) emerge as promising candidates for the next generation of solar devices, paving the way for more efficient and powerful energy solutions. The magnetic properties of $TlMCl_3$ (M = Ge, Sn) reveal a nonmagnetic (NM) nature. The inclusion of spin-orbit coupling (SOC) plays a crucial role in reducing the bandgap of $TlMCl_3$ (M = Ge, Sn) at ambient pressure, primarily by causing a downward shift in the conduction band minimum (CBM). This makes the materials highly relevant for optoelectronic applications, where a reduced bandgap can lead to improved device performance. Moreover, the materials exhibit excellent transparency, UV reflectivity, and increased absorption and conductivity under pressure, making them ideal for UV coatings, optical filters, and advanced optoelectronic devices. The mechanical analyses further support the materials' increased stiffness and ductility, with $TlSnCl_3$ showing greater machinability. Regrettably, no experimental or theoretical data are currently available on the thermodynamic properties and phonon dispersion of $TlMCl_3$ (M = Ge, Sn) compounds, making our study the first theoretical prediction in this area. Our results provide crucial insights that can guide future research and experimental validation, particularly in areas such as thermodynamic behavior and phonon stability. We believe this study will inspire the broader research community in their pursuit of halide perovskites with optimized optoelectronic properties, paving the way for innovative energy solutions and next-generation technologies.

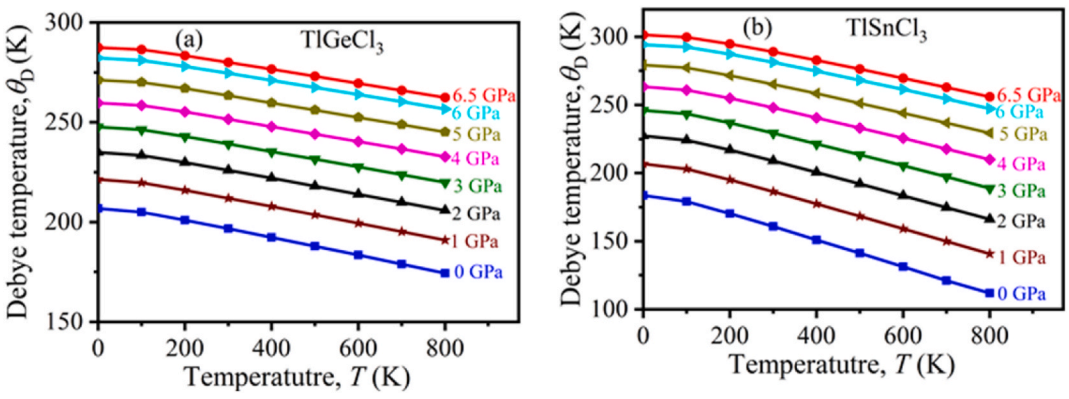

Fig. 16. The variation of Debye temperature as a function of temperature for (a) $TlGeCl_3$ and (b) $TlSnCl_3$.

CRediT authorship contribution statement

M.H. Mia: Writing – review & editing, Writing – original draft, Visualization, Validation, Supervision, Methodology, Investigation, Formal analysis, Conceptualization. **Mst.A. Khatun:** Validation, Software, Resources, Methodology, Investigation, Data curation.

Data availability

Relevant data from this study are available from the corresponding author upon a reasonable request.

Declaration of competing interest

The authors declare that they have no known competing financial interests or personal relationships that could have appeared to influence the work reported in this paper.

References

[1] W. Zhang, G.E. Eperon, H.J. Snaith, Metal halide perovskites for energy applications, Nat. Energy 1 (6) (2016) 1–8.
[2] W.J. Yin, T. Shi, Y. Yan, Unique properties of halide perovskites as possible origins of the superior solar cell performance, Adv. Mater. 26 (27) (2014) 4653–4658.
[3] C.C. Stoumpos, C.D. Malliakas, J.A. Peters, Z. Liu, M. Sebastian, J. Im, T.C. Chasapis, A.C. Wibowo, Crystal growth of the perovskite semiconductor $CsPbBr_3$: a new material for high-energy radiation detection, Cryst. Growth Des. 13 (7) (2013) 2722–2727.
[4] M. Saiduzzaman, T. Takei, S. Yanagida, N. Kumada, H. Das, H. Kyokane, S. Wakazaki, Y. Kuroiwa, Hydrothermal synthesis of pyrochlore-type pentavalent bismuthates $Ca_2Bi_2O_7$ and $Sr_2Bi_2O_7$, Inorg. Chem. 58 (3) (2019) 1759–1763.
[5] M. Saiduzzaman, H. Yoshida, T. Takei, S. Yanagida, N. Kumada, M. Nagao, H. Yamane, et al., Hydrothermal synthesis and crystal structure of a $(Ba_{0.54}K_{0.46})_4Bi_4O_{12}$ double-perovskite superconductor with onset of the transition $T_C\sim$ 30 K, Inorg. Chem. 58 (18) (2019) 11997–12001.
[6] M.H.K. Rubel, S.K. Mitro, B.K. Mondal, M.M. Rahaman, Md Saiduzzaman, J. Hossain, A.K.M.A. Islam, N. Kumada, Newly synthesized A-site ordered cubic-perovskite superconductor $(Ba_{0.54}K_{0.\ 46})_4Bi_4O_{12}$: a DFT investigation, Physica C (Amsterdam, Neth.) 574 (2020) 1353669.
[7] A. Oleaga, A. Salazar, D. Skrzypek, Critical behaviour of magnetic transitions in $KCoF_3$ and $KNiF_3$ perovskites, J. Alloys Compd. 629 (2015) 178–183.
[8] W.S. Yang, B.W. Park, E.H. Jung, N.J. Jeon, Y.C. Kim, D.U. Lee, S.S. Shin, J. Seo, E.K. Kim, J.H. Noh, Iodide management in formamidinium-lead-halide–based perovskite layers for efficient solar cells, Science 356 (6345) (2017) 1376–1379.
[9] L. Huang, W.R.L. Lambrecht, Electronic band structure trends of perovskite halides: beyond Pb and Sn to Ge and Si, Phys. Rev. B 93 (19) (2016) 195211.
[10] X. Wu, W. Song, Q. Li, X. Zhao, D. He, Z. Quan, Synthesis of lead-free $CsGeI_3$ perovskite colloidal nanocrystals and electron beam-induced transformations, Chem.–Asian J. 13 (13) (2018) 1654–1659.
[11] Y. Yuan, R. Xu, H.T. Xu, F. Hong, F. Xu, L.J. Wang, Nature of the band gap of halide perovskites ABX_3 (A= CH_3NH_3, Cs; B= Sn, Pb; X= Cl, Br, I): first-principles calculations, Chin. Phys. B 24 (11) (2015) 116302.
[12] T. Zhao, S. Zhang, Y. Guo, Q. Wang, TiC_2: a new two-dimensional sheet beyond MXenes, Nanoscale 8 (1) (2016) 233–242.
[13] M. Roknuzzaman, K.K. Ostrikov, K.C. Wasalathilake, C. Yan, H. Wang, T. Tesfamichael, Insight into lead-free organic-inorganic hybrid perovskites for photovoltaics and optoelectronics: a first-principles study, Org. Electron. 59 (2018) 99–106.
[14] K. Nishimura, M.A. Kamarudin, D. Hirotani, K. Hamada, Q. Shen, S. Iikubo, T. Minemoto, Lead-free tin-halide perovskite solar cells with 13% efficiency, Nano Energy 74 (2020) 104858.
[15] C. Grote, R.F. Berger, Strain tuning of tin–halide and lead–halide perovskites: a first-principles atomic and electronic structure study, J. Phys. Chem. C 119 (40) (2015) 22832–22837.
[16] Q.A. Akkerman, V. D'innocenzo, S. Accornero, A. Scarpellini, A. Petrozza, M. Prato, L. Manna, Tuning the optical properties of cesium lead halide perovskite nanocrystals by anion exchange reactions, J. Am. Chem. Soc. 137 (32) (2015) 10276–10281.
[17] J.L. Knutson, J.D. Martin, D.B. Mitzi, Tuning the band gap in hybrid tin iodide perovskite semiconductors using structural templating, Inorg. Chem. 44 (13) (2005) 4699–4705.
[18] O. Das, M. Saiduzzaman, K.M. Hossain, I.K. Shuvo, M.M. Rahman, S. Ahmad, S.K. Mitro, First-principles calculations to investigate pressure-driven electronic phase transition of lead-free halide perovskites $KMCl_3$ (M= Ge, Sn) for superior optoelectronic performance, Results Phys. 44 (2023) 106212.
[19] M.M. Hasan, M.A. Sarker, M.B. Mansur, M.R. Islam, S. Ahmad, Pressure-induced structural, electronic, optical, and mechanical properties of lead-free $GaGeX_3$ (X= Cl, Br and, I) perovskites: first-principles calculation, Heliyon 10 (15) (2024) e34824.
[20] M.S. Alam, M. Saiduzzaman, A. Biswas, T. Ahmed, A. Sultana, K.M. Hossain, Tuning band gap and enhancing optical functions of $AGeF_3$ (A= K, Rb) under pressure for improved optoelectronic applications, Sci. Rep. 12 (1) (2022) 8663.
[21] N.A. Noor, M. Rashid, G.M. Mustafa, M.I. Khan, Study of pressure induced physical properties of $ZnZrO_3$ perovskite using density functional theory, Chem. Phys. Lett. 753 (2020) 137601.
[22] N.A. Noor, M. Rashid, S.M. Alay-e-Abbas, M. Raza, A. Mahmood, S.M. Ramay, G. Murtaza, Shift of indirect to direct bandgap and thermoelectric response of the cubic $BiScO_3$ via DFT-mBJ studies, Mater. Sci. Semicond. Process. 49 (2016) 40–47.
[23] M. Yaseen, M.K. Butt, A. Ashfaq, J. Iqbal, M.M. Almoneef, M. Iqbal, A. Murtaza, A. Laref, Phase transition and thermoelectric properties of cubic $KNbO_3$ under pressure: DFT approach, J. Mater. Res. Technol. 11 (2021) 2106–2113.
[24] A. Batool, M.A. Faridi, Q. Mahmood, B.U. Haq, A. Laref, S.E. Awan, The pressure-induced indirect to direct bandgap transition and thermoelectric response in $SrTiO_3$: an ab-initio study, J. Phys. Chem. Solid. 123 (2018) 70–75.
[25] M.A. Islam, J. Islam, M.N. Islam, S.K. Sen, A.K.M. Hossain, Enhanced ductility and optoelectronic properties of environment-friendly $CsGeCl_3$ under pressure, AIP Adv. 11 (4) (2021).
[26] M.A. Islam, J. Islam, A.K.M. Hossain, Semiconducting to metallic transition with outstanding optoelectronic properties of $CsSnCl_3$ perovskite under pressure, Sci. Rep. 10 (1) (2020) 14391.
[27] M.A. Islam, M.Z. Rahaman, S.K. Sen, A comparative study of hydrostatic pressure treated environmentally friendly perovskites $CsXBr_3$ (X= Ge/Sn) for optoelectronic applications, AIP Adv. 11 (7) (2021).
[28] M.I. Kholil, M.T.H. Bhuiyan, Effects of pressure on narrowing the band gap, visible light absorption, and semi-metallic transition of lead-free perovskite $CsSnBr_3$ for optoelectronic applications, J. Phys. Chem. Solid. 154 (2021) 110083.
[29] M.S. Hossain, M.M. Haque Babu, T. Saha, M.S. Hossain, Pressure induced semiconductor to metal phase transition in cubic $CsSnBr_3$ perovskite, AIP Adv. 11 (5) (2021).
[30] M. Mohammed, Y. Ziat, H. Belkhanchi, Y.A. El Kadi, The effect of pressure on the structural, optoelectronic and mechanical conduct of the $XZnF_3$ (X= Na, K and Rb) perovskite: first-principles study, Int. J. Mod. Phys. B (2024) 2550096.
[31] W. Kim, B. Koo, M.J. Ko, H. Jung, Hot-injection synthesis of lead-free pseudo-alkali metal-based perovskite ($TlSnX_3$) nanoparticles with tunable optical properties, Front. Mater. 10 (2023) 1298188.

[32] J.K. Rony, M. Islam, M. Saiduzzaman, K.M. Hossain, S. Alam, A. Biswas, M.H. Mia, S. Ahmad, S.K. Mitro, $TlBX_3$ (B= Ge, Sn; X= Cl, Br, I): promising non-toxic metal halide perovskites for scalable and affordable optoelectronics, J. Mater. Res. Technol. 29 (2024) 897–909.
[33] P. Sharma, P. Ranjan, T. Chakraborty, Study of Tl-based perovskite materials $TlZX_3$ (Z= Ge, Sn, Be, Sr; X= Cl, Br, I) for application in scintillators: DFT and TD-DFT approach, Chemical Physics Impact 7 (2023) 100344.
[34] A. Marjaoui, M. Ait Tamerd, M. Zanouni, Semiconducting-metallic phase transition with tunable optoelectronics and mechanical properties of halide perovskites $TlGeX_3$ (X= F, Cl) under pressure, J. Mater. Sci. Mater. Electron. 34 (36) (2023) 2327.
[35] S. Bouhmaidi, M.B. Uddin, R.K. Pingak, S. Ahmad, et al., Investigation of heavy thallium perovskites TlGeX3 (X= Cl, Br and I) for optoelectronic and thermoelectric applications: a DFT study, Mater. Today Commun. 37 (2023) 107025.
[36] R.K. Pingak, A.Z. Johannes, N.U.J. Hauwali, U.A. Deta, Lead-free perovskites $TlGeCl_xBr_{3-x}$ (X= 0, 1, 2, 3) as promising materials for solar cell application: a DFT study, J. Phys. Conf. 2623 (1) (2023) 012002.
[37] M.D. Segall, P.J.D. Lindan, M.J. Probert, C.J. Pickard, P.J. Hasnip, S.J. Clark, M.C. Payne, First-principles simulation: Ideas, illustrations and the CASTEP code, J. Phys. Condens. Matter 14 (11) (2002) 2717.
[38] M.C. Payne, M.P. Teter, D.C. Allan, T.A. Arias, J.D. Joannopoulos, Iterative minimization techniques for ab initio total-energy calculations: molecular dynamics and conjugate gradients, Rev. Mod. Phys. 64 (4) (1992) 1045.
[39] J.P. Perdew, K. Burke, M. ErnzerhofGeneralized, Gradient approximation made simple, Phys. Rev. Lett. 77 (18) (1996) 3865.
[40] H.J. Monkhorst, J.D. Pack, Special points for brillouin-zone integrations, Phys. Rev. B 13 (12) (1976) 5188.
[41] D. Vanderbilt, Soft self-consistent pseudopotentials in a generalized eigenvalue formalism, Phys. Rev. B 41 (11) (1990) 7892.
[42] T.H. Fischer, J. Almlof, General methods for geometry and wave function optimization, The Journal of Physical Chemistry 96 (24) (1992) 9768–9774.
[43] Y. Pan, M. Wen, Noble metals enhanced catalytic activity of anatase TiO_2 for hydrogen evolution reaction, Int. J. Hydrogen Energy 43 (49) (2018) 22055–22063.
[44] R.K. Pingak, S. Bouhmaidi, L. Setti, B. Pasangka, B. Bernandus, H.I. Sutaji, F. Nitti, M.Z. Ndii, Structural, electronic, elastic, and optical properties of cubic $BaLiX_3$ (X= F, Cl, Br, or I) perovskites: an ab-initio DFT study, Indones.J. Chem. 23 (3) (2023) 843–862.
[45] F. Tran, P. Blaha, Accurate band gaps of semiconductors and Insulators<? Format?> with a semilocal exchange-correlation potential, Phys. Rev. Lett. 102 (22) (2009) 226401.
[46] M. Wuttig, C.F. Schön, M. Schumacher, J. Robertson, P. Golub, E. Bousquet, C. Gatti, J.Y. Raty, Halide perovskites: advanced photovoltaic materials empowered by a unique bonding, Mech. Adv. Funct. Mater. 32 (2) (2022) 2110166.
[47] M.A. Rashid, M. Saiduzzaman, A. Biswas, K.M. Hossain, First-principles calculations to explore the metallic behavior of semiconducting lead-free halide perovskites RbSnX3 (X= Cl, Br) under pressure, Eur. Phys. J. Plus 137 (6) (2022) 649.
[48] S.K. Mitro, M. Saiduzzaman, T.I. Asif, K.M. Hossain, Band gap engineering to stimulate the optoelectronic performance of lead-free halide perovskites $RbGeX_3$ (X= Cl, Br) under pressure, J. Mater. Sci. Mater. Electron. 33 (17) (2022) 13860–13875.
[49] M.A. Haq, M. Saiduzzaman, T.I. Asif, I.K. Shuvo, Ultra-violet to visible band gap engineering of cubic halide $KCaCl_3$ perovskite under pressure for optoelectronic applications: insights from DFT, RSC Adv. 11 (58) (2021) 36367–36378.
[50] I.K. Shuvo, M. Saiduzzaman, T.I. Asif, M.A. Haq, Band gap shifting of halide perovskite $CsCaBr_3$ from ultra-violet to visible region under pressure for photovoltaic applications, Mater. Sci. Eng., B 278 (2022) 115645.
[51] F.D. Murnaghan, The compressibility of media under extreme pressures, Proc. Natl. Acad. Sci. USA 30 (1944) 244.
[52] Mst A. Khatun, M.H. Mia, M.A. Hossain, F. Parvin, A.K.M.A. Islam, Optical and thermoelectric properties of layer structured Ba_2XS_4 (X= Zr, Hf) for energy harvesting applications, J. Phys. Chem. Solid. 196 (2025) 112381.
[53] M.M. Saad, S.E.A. Yousif, Structural and optoelectronic properties of $CsSnBr_3$ metal halide perovskite as promising materials toward novel-generation optoelectronics, Chalcogenide Lett. 19 (2) (2022).
[54] B.O. Alsobhi, A. Almeshal, Tuning of band gap and enhancing electronic properties of $CsSnBr_3$ under high pressure for optoelectronic applications, Comput. Condens. Matter 38 (2024) e00870.
[55] M.H. Mia, Mst A. Khatun, M. Rahman, Ti_2PTe_2 chalcogenide: a comprehensive DFT study on physical properties, Materials 7 (2025) 100434.
[56] S. Körbel, M.A.L. Marques, S. Botti, Stability and electronic properties of new inorganic perovskites from high-throughput ab initio calculations, J. Mater. Chem. C 4 (15) (2016) 3157–3167.
[57] A.D. Becke, E.R. Johnson, A simple effective potential for exchange, J. Chem. Phys. 124 (22) (2006).
[58] N.A. Noor, M. Hassan, M. Rashid, S.M. Alay-e-Abbas, A. Laref, Systematic study of elastic, electronic, optical and thermoelectric properties of cubic $BiBO_3$ and $BiAlO_3$ compounds at different pressure by using ab-initio calculations, Mater. Res. Bull. 97 (2018) 436–443.
[59] N.A. Noor, N. Ikram, S. Ali, S. Nazir, S.M. Alay-e-Abbas, A. Shaukat, First-principles calculations of structural, electronic and optical properties of $Cd_xZn_{1-x}S$ alloys, J. Alloys Compd. 507 (2) (2010) 356–363.
[60] M. Hassan, A. Shahid, Q. Mahmood, Structural, electronic, optical and thermoelectric investigations of antiperovskites A_3SnO (A= Ca, Sr, Ba) using density functional theory, Solid State Commun. 270 (2018) 92–98.
[61] R.K. Pingak, S. Bouhmaidi, A. Harbi, L. Setti, F. Nitti, M. Moutaabbid, A.Z. Johannes, N.U.J. Hauwali, A DFT investigation of lead-free $TlSnX_3$ (X= Cl, Br, or I) perovskites for potential applications in solar cells and thermoelectric devices, RSC Adv. 13 (48) (2023) 33875–33886.
[62] A.P. Nayak, S. Bhattacharyya, J. Zhu, J. Liu, X. Wu, T. Pandey, C. Jin, A.K. Singh, D. Akinwande, Pressure-induced semiconducting to metallic transition in multilayered molybdenum disulphide, Nat. Commun. 5 (1) (2014) 1–9.
[63] X. Chen, L. Zhang, J. Cui, X. Meng, J. Liu, S. Yao, G. Chen, Z. Shen, F. Du, Semiconductor-to-metal transition renders intrinsic pseudocapacitance and high volumetric capacity for iron chalcogenide anode, Chem. Eng. J. 480 (2024) 147979.
[64] A.C.M. Esther, G.M. Muralikrishna, M. Chirumamilla, M.S. Pinto, S. Ostendorp, M. Peterlechner, et al., Demystifying the semiconductor-to-metal transition in amorphous vanadium pentoxide: the role of substrate/thin film interfaces, Adv. Funct. Mater. 34 (30) (2024) 2309544.
[65] R.K. Pingak, A DFT study of structural and electronic properties of cubic thallium based fluoroperovskites $TlBF_3$ (B=Ge, Sn, Pb, Zn, Cd, Hg, Mg, Ca, Sr, Ba), Comput. Condens. Matter 33 (2022) E00747.
[66] R.K. Pingak, A. Harbi, S. Bouhmaidi, A.Z. Johannes, et al., Novel Tl_2GeX_6 (X= Cl, Br) double perovskites for solar cell, optoelectronic, and thermoelectric applications: a DFT investigation, Chemical Physics Impact 9 (2024) 100749.
[67] X. Song, Y. Zhao, X. Wang, J. Ni, S. Meng, Z. Dai, Strong anharmonicity and high thermoelectric performance of cubic thallium-based fluoride perovskites $TlXF_3$ (X= Hg, Sn, Pb), Phys. Chem. Chem. Phys. 25 (7) (2023) 5776–5784.
[68] A.K. Al-Mousoi, M.K.A. Mohammed, A. Kumar, R. Pandey, J. Madan, D. Dastan, M.K. Hossain, P. Sakthivel, Z. Mundher Yaseen, Understanding auger recombination in perovskite solar cells, Phys. Chem. Chem. Phys. 25 (24) (2023) 16459–16468.
[69] T. Saha, M.M.H. Babu, M. Arifuzzaman, J. Podder, Thermodynamic and dynamic stability in a new potential $Cs_2AgAsCl_6$ perovskite: insight from DFT study, Phys. Chem. Chem. Phys. 24 (43) (2022) 26609–26621.
[70] Z. Hou, Y. Xiao, L.D. Zhao, Investigation on carrier mobility when comparing nanostructures and bands manipulation, Nanoscale 12 (24) (2020) 12741–12747.
[71] W.L. Bade, Drude-model calculation of dispersion forces. I. General theory, J. Chem. Phys. 27 (6) (1957) 1280–1284.
[72] W. Wunderlich, H. Ohta, K. Koumoto, Enhanced effective mass in doped $SrTiO_3$ and related perovskites, Phys. B Condens. Matter 404 (16) (2009) 2202–2212.
[73] J. Feng, B. Xiao, Effective masses and electronic and optical properties of nontoxic $MASnX_3$ (X= Cl, Br, and I) perovskite structures as solar cell absorber: a theoretical study using HSE06, J. Phys. Chem. C 118 (34) (2014) 19655–19660.
[74] S. Mahmud, M.A. Ali, M.M. Hossain, M.M. Uddin, DFT aided prediction of phase stability, optoelectronic and thermoelectric properties of A_2AuScX_6 (A= Cs, Rb; X= Cl, Br, I) double perovskites for energy harvesting technology, Vacuum 221 (2024) 112926.
[75] L.E. Ramos, L.K. Teles, L.M.R. Scolfaro, J.L.P. Castineira, A.L. Rosa, J.R. Leite, Structural, electronic, and effective-mass properties of silicon and zinc-blende group-III nitride semiconductor compounds, Phys. Rev. B 63 (16) (2001) 165210.

[76] M. Sohail, M. Husain, N. Rahman, K. Althubeiti, M. Algethami, A.A. Khan, A. Iqbal, A. Ullah, First-principal investigations of electronic, structural, elastic and optical properties of the fluoroperovskite $TlLF_3$ (L= Ca, Cd) compounds for optoelectronic applications, RSC Adv. 12 (12) (2022) 7002–7008.
[77] S.U. Zaman, S. Khan, N. Mehmood, A.U. Rahman, R. Ahmad, N. Sultan, F. Ullah, H.J. Kim, Heavy thallium based fluoroperovskite $Tlaf_3$ (A= Ge, Sn and Pb) compounds: a computational investigation, Opt. Quant. Electron. 54 (7) (2022) 396.
[78] S. Khan, S.U. Zaman, R. Ahmad, N. Mehmood, M. Arif, H.J. Kim, Ab initio investigations of structural, elastic, electronic and optical properties of the fluoroperovskite $TlXF_3$ (X= Ca, Cd, Hg, and Mg) compounds, Mater. Res. Express 6 (12) (2020) 125923.
[79] M. Husain, N. Rahman, R. Khan, M. Sohail, A.A. Khan, H.O. Elansary, T.K.Z. El-Abedin, et al., Exploring the exemplary structural, electronic, optical, and elastic nature of inorganic ternary cubic $XBaF_3$ (X= Al and Tl) employing the accurate TB-mBJ approach, Semicond. Sci. Technol. 37 (7) (2022) 075004.
[80] M.F. Rahman, M.A. Rahman, M.R. Islam, A. Ghosh, et al., Unraveling the strain-induced and spin–orbit coupling effect of novel inorganic halide perovskites of Ca_3AsI_3 using DFT, AIP Adv. 13 (8) (2023) 085329.
[81] M. Hussain, M. Rashid, F. Saeed, A.S. Bhatti, Spin–orbit coupling effect on energy level splitting and band structure inversion in $CsPbBr_3$, J. Mater. Sci. 56 (1) (2021) 528–542.
[82] J. Even, L. Pedesseau, J.M. Jancu, C. Katan, Importance of spin–orbit coupling in hybrid organic/inorganic perovskites for photovoltaic applications, J. Phys. Chem. Lett. 4 (17) (2013) 2999–3005.
[83] N.V. Smith, Photoelectron energy spectra and the band structures of the noble metals, Phys. Rev. B 3 (6) (1971) 1862.
[84] C. Ambrosch-Draxl, J.O. Sofo, Linear optical properties of solids within the full-potential linearized augmented planewave method, Comput. Phys. Commun. 175 (1) (2006) 1–14.
[85] M.A. Hadi, R.V. Vovk, A. Chroneos, Physical properties of the recently discovered $Zr_2(Al_{1-x}Bi_x)C$ MAX phases, J. Mater. Sci. Mater. Electron. 27 (2016) 11925–11933.
[86] R. Yadav, A. Srivastava, J.A. Abraham, R. Sharma, First-principles calculations to investigate structural, electronic, thermoelectric, and optical properties of heavy thallium perovskite $TlPbX_3$ (X= Cl, Br, I), Mater. Sci. Eng., B 283 (2022) 115781.
[87] S. Khan, A. Gassoumi, A.U. Rahman, F. Ullah, R. Ahmad, N. Mehmood, M. Abdul, A.H. Shah, A first-principles study of electronic, optical and thermoelectric properties of $TlXF_3$ (X: Zn, Sr) perovskite crystal structure, Physica Scripta 98 (5) (2023) 055907.
[88] H. Joshi, D.P. Rai, L. Hnamte, A. Laref, R.K. Thapa, A theoretical analysis of elastic and optical properties of half heusler MCoSb (M= Ti, Zr and Hf), Heliyon 5 (3) (2019) e01155.
[89] H.H. Hegazy, G.M. Mustafa, A. Nawaz, N.A. Noor, A. Dahshan, I. Boukhris, Tuning of direct bandgap of Rb_2ScTlX_6 (X= Cl, Br, I) double perovskites through halide ion substitution for solar cell devices, J. Mater. Res. Technol. 19 (2022) 1271–1281.
[90] S.A. Dar, B. Want, DFT study of structural, mechanical, and opto-electronic properties of scadium-based halide double perovskite $Cs_2ScInBr_6$ for optoelectronic applications, Micro Nanostruct. 170 (2022) 207370.
[91] N.A. Noor, Q. Mahmood, M. Rashid, B.U. Haq, A. Laref, The pressure-induced mechanical and optoelectronic behavior of cubic perovskite $PbSnO_3$ via ab-initio investigations, Ceram. Int. 44 (12) (2018) 13750–13756.
[92] F. Mouhat, F.X. Coudert, Necessary and sufficient elastic stability conditions in various crystal systems, Phys. Rev. B 90 (22) (2014) 224104.
[93] M. Roknuzzaman, K. Ostrikov, H. Wang, A. Du, T. Tesfamichael, Towards lead-free perovskite photovoltaics and optoelectronics by ab-initio simulations, Sci. Rep. 7 (1) (2017) 14025.
[94] W. Voigt, Lehrbuch Der Kristallphysik (Textbook of Crystal Physics), BG Teubner, Leipzig Und Berlin, 1928.
[95] A. Reuß, Berechnung Der Fließgrenze von Mischkristallen Auf Grund Der Plastizitätsbedingung Für Einkristalle, ZAMM-Journal of Applied Mathematics and Mechanics/Zeitschrift Für Angewandte, Mathematik Und Mechanik 9 (1) (1929) 49–58.
[96] R. Hill, The elastic behaviour of a crystalline aggregate, Proc. Phys. Soc. 65 (5) (1952) 349.
[97] M. Al-Fahdi, A. Rodriguez, T. Ouyang, M. HuHigh-Throughput, Computation of new carbon allotropes with diverse hybridization and ultrahigh hardness, Crystals 11 (7) (2021) 783.
[98] G. Vaitheeswaran, V. Kanchana, A. Svane, A. Delin, Elastic properties of $MgCNi_3$—a superconducting perovskite, J. Phys. Condens. Matter 19 (32) (2007) 326214.
[99] A. Biswas, M.S. Alam, A. Sultana, T. Ahmed, M. Saiduzzaman, K.M. Hossain, Effects of Bi and Mn Co doping on the physical properties of barium titanate: investigation via DFT method, Appl. Phys. A 127 (12) (2021) 939.
[100] S.F. Pugh, Xcii. Relations between the elastic moduli and the plastic properties of polycrystalline pure metals, London, Edinburgh Dublin Phil. Mag. J. Sci. 45 (367) (1954) 823–843.
[101] D.G. Pettifor, Theoretical predictions of structure and related properties of intermetallics, Mater. Sci. Technol. 8 (4) (1992) 345–349.
[102] X. Li, F.R. Chen, Y. Lu, Ductile inorganic semiconductors for deformable electronics, Interdiscipl. Mater. 3 (6) (2024) 835–846.
[103] C.M. Zener, S. Siegel, Elasticity and anelasticity of metals, The Journal of Physical Chemistry 53 (9) (1949) 1468.
[104] M.H.K. Rubel, M.A. Hossain, M.K. Hossain, K.M. Hossain, A.A. Khatun, M.M. Rahaman, M.F. Rahman, First-principles calculations to investigate structural, elastic, electronic, thermodynamic, and thermoelectric properties of $CaPd_3B4O_{12}$ (B= Ti, V) perovskites, Results Phys. 42 (2022) 105977.
[105] A.R. Oganov, J.P. Brodholt, G.D. Price, Comparative study of quasiharmonic lattice dynamics, molecular dynamics and Debye model applied to $MgSiO_3$ perovskite, Phys. Earth Planet. Inter. 122 (3) (2000) 277–288.
[106] X. Liu, J. Fu, M.M. Han, K.X. Sun, S.L. Wei, First-principles study on electronic structure, elasticity, Debye temperature and anisotropy of cubic $KCaF_3$, Mater. Sci. Forum 999 (2020) 109–116.
[107] S.C. Mouna, M. Radjai, A. Bouhemadou, D. Houatis, D. Allali, S.S. Essaoud, S. Bin-Omran, Structural, elastic, and thermodynamic properties of $BaXCl_3$ (X= Li, Na) perovskites under pressure effect: ab initio exploration, Physica Scripta 98 (6) (2023) 065949.